



Selective reduction of nitrobenzene to aniline over electrocatalysts based on nitrogen-doped carbons containing non-noble metals

Nick Daems^a, Jonatan Wouters^a, Cédric Van Goethem^a, Kitty Baert^b, Claude Poleunis^c, Arnaud Delcorte^c, Annick Hubin^b, Ivo F.J. Vankelecom^a, Paolo P. Pescarmona^{a,d,*}

^a Centre for Surface Chemistry and Catalysis, KU Leuven, Celestijnenlaan 200F, 3001 Heverlee, Belgium

^b Research Group Electrochemical and Surface Engineering, Vrije Universiteit Brussel, Pleinlaan 2, 1050 Brussels, Belgium

^c PCPM, Université Catholique de Louvain, Croix du Sud 1, 1348 Louvain-la-Neuve, Belgium

^d Chemical Engineering Group, Engineering and Technology Institute Groningen (ENTEG), University of Groningen, Nijenborgh 4, 9749 AG, Groningen, The Netherlands



ARTICLE INFO

Keywords:

Cogeneration
Fuel cell
Aniline
Non-noble metals
N-doped carbon

ABSTRACT

Non-noble metals (Fe, Co or Cu) supported on N-doped carbons were investigated for the first time as electrocatalysts for the reduction of nitrobenzene to aniline in a half-cell setup. The electrocatalysts were prepared by pyrolysis of composites of activated carbon (AC) and polyaniline (PANI) with incorporated metal sites. The electrocatalyst performance was strongly influenced by the nature of the metal and by the synthesis method. For the latter, a different optimum was identified for each metal. The Cu-based electrocatalyst synthesised with a low amount of PANI and Cu relative to AC, was identified as the best electrocatalyst based on its onset potential, kinetic current density and selectivity to aniline. Most importantly, unprecedented selectivity to aniline was obtained (82%, as determined by chronoamperometry) with this electrocatalyst in a half-cell setup. This makes it a promising candidate for the electrochemical cogeneration of the industrially valuable aniline and electricity in a proton-exchange membrane fuel cell.

1. Introduction

Aniline is an important industrial chemical product [1], which is largely employed as reagent for the synthesis of polyurethane [2]. In 2010, the world aniline production was ca. $2.3 \cdot 10^6$ tons, of which 2/3 was utilised in the production of polyurethane [3]. Currently, aniline is mainly produced through the hydrogenation of nitrobenzene with Raney nickel or other nickel alloys as catalyst [1,4,5]. In order to achieve sufficiently high conversion and selectivity towards aniline (currently between 80 and 90%, with azobenzene and azoxybenzene as the main side-products), the reaction is performed at 35–125 °C, at high H₂ pressure (≥ 0.6 MPa) and with long reaction times [1,2,4,5]. Furthermore, since this hydrogenation reaction is exergonic ($\Delta_r G^\circ < 0$), a high amount of heat is typically lost in the process. In general, safe heat removal can be challenging and might lead to reactor hot spots, lowering the reaction yields [6,7].

An attractive, green alternative to this process could be provided by an electrochemical approach, where aniline is produced at room temperature in a fuel cell and the chemical energy liberated by the reaction is converted into electricity. In this way, the synthesis of a valuable

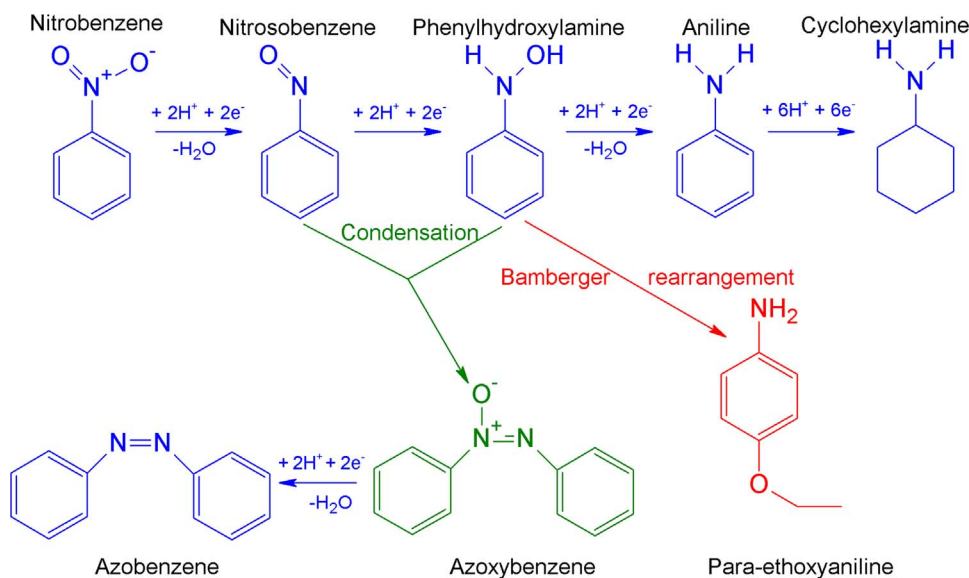
product like aniline can be coupled with electricity generation, giving rise to a more sustainable and more energy-efficient process [8,9]. Moreover, the electrochemical aniline production would offer the possibility to control the reaction rate and the selectivity by tuning the electrical potential [10]. For this route to become competitive with the current industrial production, research should be dedicated to the development of an active, selective, stable and affordable electrocatalyst, which is the focus of this work, of an efficient and cost-effective membrane, and to the assembly of these components into a fuel cell [11,12].

The possibility to reduce nitrobenzene electrochemically was first investigated by Haber et al. and has been further developed since then [7–9,13]. The electrochemical cell typically consists of an anodic and a cathodic compartment, which are separated by a proton exchange membrane (PEM). At the anode, protons and free electrons are generated from the oxidation of hydrogen. Both flow to the cathodic compartment, the electrons through an external circuit and the protons through the PEM. Once they reach the cathode, they are involved in the reduction of nitrobenzene. The overall reactions are:

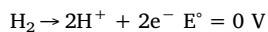
Anode:

* Corresponding author at: Chemical Engineering Group, Engineering and Technology Institute Groningen (ENTEG), University of Groningen, Nijenborgh 4, 9749 AG, Groningen, The Netherlands.

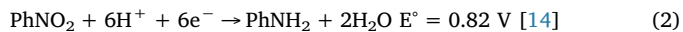
E-mail address: p.p.pescarmona@rug.nl (P.P. Pescarmona).



Scheme 1. Reaction scheme of the reduction of nitrobenzene.



Cathode:



However, the full reaction scheme is more complex and can involve both electrochemical and chemical steps [7–9,15]. It is generally accepted that the reduction of nitrobenzene to aniline consists of two main steps: first, nitrobenzene is reduced to phenylhydroxylamine (PHA) through a 4-electron exchange, with nitrosobenzene (NSB) as an intermediate. Then, a 2-electron reduction step converts PHA to aniline (Scheme 1) [16,17]. Nitrosobenzene is generally not detected since it is rapidly converted to PHA via a second 2-electron reduction [17]. PHA is a very unstable compound and, besides being reduced to give aniline, it can also react further through three competitive chemical reactions, leading to the formation of side-products as azoxybenzene, azobenzene and para-ethoxyaniline (Scheme 1). These competitive reactions have already been discussed in detail elsewhere [7–9,18–20]. If aniline is obtained through the electrochemical reduction of nitrobenzene, care should be taken to avoid further reduction to cyclohexylamine. The formation of this side-product has been reported to take place on carbon-supported platinum (Pt/C) electrocatalysts in a fuel cell [21].

The outcome of the nitrobenzene reduction is strongly influenced by the employed electrocatalyst [7,16,17,19,22–26] and by the reaction conditions, such as the electrode potential [17,19,24] and the pH of the electrolyte solution [16,23,24,27]. It has already been demonstrated that the selectivity towards aniline can be increased by applying more negative electrode potentials. However, an optimal potential exists since the possibility to further reduce aniline towards cyclohexylamine becomes more likely at increasingly negative potentials. Furthermore, at these potentials the Faradaic efficiency towards the reduction of nitrobenzene is decreased by a competing reaction, i.e. the hydrogen evolution [17,24]. The effect of the pH was investigated previously and it was determined that nitrosobenzene is detected in alkaline environments, suggesting slower reaction kinetics [27] and that the 2-electron reduction step to form PHA is strongly hindered in alkaline environment compared to acidic or neutral environments [7,24]. In this work, the electrochemical reduction of nitrobenzene was investigated in acidic (HClO_4) ethanolic environment, in a half-cell setup by means of linear sweep voltammetry (LSV) and chronoamperometry.

The nature of the electrocatalyst used at the cathode has a crucial impact on the nitrobenzene reduction rate and at the same time on the selectivity of the reaction. Therefore, the development of efficient and

cost-effective electrocatalysts is of utmost importance for enabling the practical application of the electrochemical route to produce aniline with cogeneration of electricity. Commonly used cathode electrocatalysts for this specific reaction are noble metals like Pt, Pd, or Au supported on activated carbon or carbon nanotubes [7,9,21,25]. Even if these materials offer a good activity and stability, their high cost is a drawback, which limits commercialisation [7,17,24]. Non-noble metals such as Cu or Fe have been identified as less expensive alternatives to the noble metals but in an electrochemical approach they do not reach sufficiently high selectivities to aniline [7,24,26]. Recently, it was demonstrated that the presence of a metal is not strictly necessary as N-doped diamond [24] was shown to be an efficient electrocatalyst for the production of aniline from nitrobenzene. A drawback of N-doped diamond is that it is synthesised through chemical vapour deposition, which requires severe conditions and implies a high production cost [12]. In order to make the electrochemical cogeneration approach economically viable, more research is necessary to further enhance the selectivity to the target product, aniline, and this in combination with a reduction of the electrocatalyst manufacturing costs.

In this work, non-noble metals (Fe, Co or Cu) supported on N-doped carbons were investigated for the first time as electrocatalysts for the cogeneration of aniline and electricity. Iron, cobalt and copper were chosen as metal species in the electrocatalysts because they are affordable and abundant and they have several accessible oxidation states, which can be beneficial to promote the reduction reaction. Previous work by our group already investigated the use of supported copper nanoparticles as electrocatalysts for the nitrobenzene reduction reaction [7–9]. However, since the selectivity was still low, further improvements were required. Therefore, in this work it is proposed to replace the multi-walled carbon nanotubes as a support by N-doped carbons. The nitrogen doping is expected to enhance the electrocatalytic performance by generating extra active sites for the nitrobenzene reduction (N-doping generates partially positively charged carbon atoms, which might act as active sites) [12] and by improving the interaction between metal and support (possibly enhancing electron exchange). Inspired by our previous observations that Cu outperformed Pt as a consequence of its more electropositive behaviour, iron and cobalt, which are both more electropositive than copper, were chosen as alternative metals in an attempt to further enhance the reduction performance [7]. Our design of catalysts also shows a relationship to recent developments in the chemical reduction of nitrobenzene over heterogeneous catalysts, in which N-doped carbons with different morphologies were employed as support for noble and non-noble

metals [28,29] and even as metal-free catalysts [30]. The work reported here combined the electrochemical investigation and physicochemical characterisation of the prepared noble-metal-free materials and led to the identification of novel electrocatalysts for the reduction of nitrobenzene with remarkably high selectivity towards the desired aniline product.

2. Experimental

2.1. Materials

The following chemicals were used in this work: aniline (99.8%, pure, Acros Organics), activated carbon Norit® SX1G ($878 \text{ m}^2 \text{ g}^{-1}$, Norit Americas inc.), iron(III) chloride (97%, reagent grade, Sigma Aldrich), copper(II) chloride (99%, extra pure, anhydrous, Acros Organics), cobalt(II) chloride hexahydrate (98%, reagent grade, Sigma Aldrich), ammonium peroxydisulphate (98%, Acros Organics), sulphuric acid ($> 95\%$, Fisher Chemical), hydrochloric acid (37% aqueous solution, Fisher Chemical), perchloric acid (70% aqueous solution, Sigma Aldrich), nitrobenzene ($\geq 99\%$, Sigma Aldrich) and phosphate buffer (pH = 7, Fisher). All these chemicals were used as received from commercial sources.

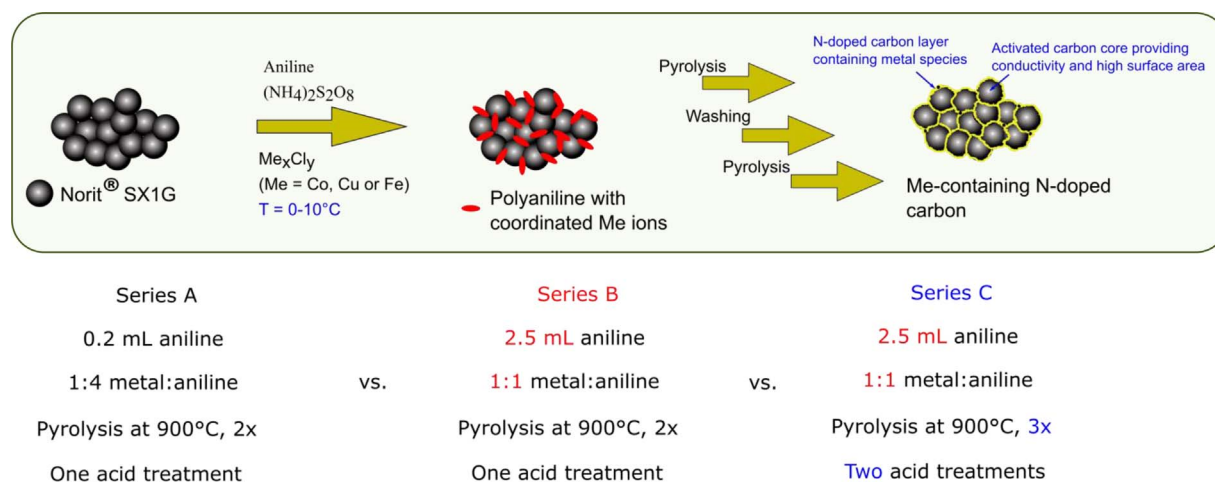
2.2. Synthesis of the electrocatalysts

Metal-containing N-doped carbon materials were prepared through procedures inspired by a previously reported method (Scheme 2) [10,31]. In the first step, activated carbon (AC) was treated with a 6 M HCl aqueous solution for 24 h at room temperature to remove impurities. Next, 0.5 g of the purified activated carbon was suspended in 0.5 M HCl at a temperature between 0 and 10 °C. After 15 min, aniline (0.2 or 2.5 mL) was added and after an additional hour, ammonium peroxydisulphate (APS) $(\text{NH}_4)_2\text{S}_2\text{O}_8$, as oxidant (1.2:1 molar ratio relative to aniline), and the metal precursor, (1:1 or 1:4 molar ratio relative to aniline) were added to the synthesis mixture. This suspension was stirred for 24 h. Next, the solvent was evaporated under reduced pressure and the remaining solid was further dried in a vacuum oven at 80 °C overnight. Then, the material was subjected to a first pyrolysis under N_2 at 900 °C for 1 h at a heating rate of $3.3 \text{ }^{\circ}\text{C min}^{-1}$. Afterwards, the solid was treated in 0.5 M sulphuric acid at 80 °C for 8 h to remove unstable surface species, followed by filtration, washing with deionised water and drying in a vacuum oven. Finally, the material was subjected to a second pyrolysis for 3 h at 900 °C in order to reduce species that were oxidised during the acid treatment. Three different sets of electrocatalysts were prepared, each with the three different metals (Cu, Co or Fe): (1) Me-PANI-AC-A with 0.2 mL aniline and a metal-to-aniline

ratio of 1:4 in the synthesis mixture; (2) Me-PANI-AC-B with 2.5 mL aniline and a metal-to-aniline ratio of 1:1 and (3) Me-PANI-AC-C, same composition as Me-PANI-AC-B but with a second acid treatment and a third pyrolysis step of 3 h, to investigate the efficiency of the applied acid treatment to remove unstable metal species (Scheme 2). The aniline-to-APS ratio was kept constant for the three sets, resulting in a higher APS/metal ratio for the latter two sets of electrocatalysts. As a reference, a metal-free material was prepared according to the procedure of series A (PANI-AC-A).

2.3. Physicochemical characterisation

A STOE Stadi P Combi instrument was used in transmission mode to measure the X-ray diffraction (XRD) patterns. The instrument was used in high-throughput mode and was equipped with a $\text{Cu}-\text{K}\alpha$ radiation source ($\lambda = 1.54 \text{ \AA}$) and a $\text{K}\alpha 1$ Germanium Johann-type monochromator. A high-throughput image plate position detector (IP-PSD) from STOE was used as detector. The XRD instrument was controlled by WinXPOW version 2.20 software from STOE and all the measurements were performed in the 2θ range from 0 to 75°. Nitrogen adsorption-desorption isotherms were measured at 77 K on a Micromeritics Tristar 3000. The pore size distributions were determined using the Barrett-Joyner-Halenda (BJH) method, whereas the Brunauer-Emmett-Teller (BET) method was used to calculate the surface area of the samples. Thermogravimetric analysis (TGA) was performed to determine the metal content. The measurements were carried out under O_2 flow on a TGA Q500 from TA instruments. The temperature was ramped with a heating rate of $5 \text{ }^{\circ}\text{C min}^{-1}$ until 1000 °C was reached, and then it was held constant until the mass change was smaller than 0.05 \% min^{-1} , after which the system was cooled down to room temperature. Previous XRD studies showed that the residual red-orange powder is Fe_2O_3 for the Fe-containing samples [32]. In the case of Cu and Co, XRD showed that the residual powder is CuO and CoO , respectively. The residual mass can thus be used to determine the overall metal content of the sample. Since peaks that could be assigned to trace amounts of quartz wool, which was used during the pyrolysis, could also be detected in the XRD pattern of our materials, the metal content determined by TGA is a slight overestimation of the actual value. X-ray photoelectron spectroscopy (XPS) measurements were performed on a Physical Electronics PHI 1600 multi-technique system using an $\text{Al K}\alpha$ (1486.6 eV) monochromatic X-ray source, which was operated at 15 kV and 150 W at a base pressure of $2 \cdot 10^{-9}$ Torr. The graphitic C 1 s band at 284.6 eV was taken as internal standard, in order to correct possible deviations caused by electric charging of the samples. The MultiPak software was used for the deconvolution and integration of the XPS signals. Room-temperature Raman spectra were recorded on a LabRAM HR Evolution



Scheme 2. Synthesis of the Me-PANI-AC electrocatalysts and summary of the synthesis conditions of the different series of electrocatalysts.

spectrometer from HORIBA Scientific. The spectrometer was equipped with a high stability confocal microscope with XYZ motorized stage and objectives of 10 × 50x, 100x magnification, a multichannel air cooled detector (with a spectral resolution of < 1 cm⁻¹) and a solid state laser at a wavelength of 532 nm (Nd:YAG). Deconvolution and peak integration was performed by using the IgorPro software. Transmission electron microscopy (TEM) and scanning transmission electron microscopy (STEM) images were recorded on a JEOL Atomic Resolution Microscope (ARM-200F), equipped with a cold FEG and operated at 200 kV. The high-angle annular dark-field scanning transmission electron microscopy (HAADF-STEM) images were recorded at an angle of 6.8 mrad semi-angle (inner diameter) and 28 mrad semi-angle (outer diameter). The microscope is equipped with an energy dispersive X-ray (EDX) spectrometer to perform EDX measurements at a collection angle of 0.98 sr and with a 100 mm² detection area. Time of Flight Secondary Ion Mass Spectroscopy (ToF-SIMS) was carried out on an IONTOF V instrument (IONTOF, GmbH, Münster, Germany). Sample powders were manually pressed with a spatula onto the adhesive part of Post-it® papers. A pulsed Bi⁵⁺ or Bi³⁺ metal ion source was used to produce a primary beam using an acceleration voltage of 30 kV. An AC target current of 0.06 pA with a bunched pulse width lower than 1.5 ns was used. The analysis was conducted on the positive and negative secondary ion species. For the spectra, a raster of 128 × 128 data points over an area of 150 × 150 μm² was used. The total primary ion beam dose for each analysed area was always kept below 10¹¹ ions·cm⁻², ensuring static conditions. Lateral resolution of ~3 μm and mass resolution m/Δm > 5000 at 29 m/z were maintained for positive and negative spectra acquisition. Charge compensation was done by interlaced electron flood gun (E_k = 20 eV). All data analyses were carried out using the software supplied by the instrument manufacturer, SurfaceLab (version 6.5). It is worth mentioning here that ToF-SIMS is a semi-quantitative technique. It can thus be applied to determine the different species present in the material and their relative abundancies, but it does not offer the possibility to quantify their absolute amounts (for this purpose XPS is used here) [33].

2.4. Electrochemical characterisation

All electrochemical measurements were carried out in a three-electrode half-cell setup using a Gamry Interface 1000E potentiostat. Analysis of the products after chronoamperometry was performed using gas chromatography (GC) on a Shimadzu 2010 Plus equipped with a Rtx-5 amine-functionalised standard capillary column (15 m, 0.25 mm internal diameter). For all the electrochemical measurements, glassy carbon porous rotating disk electrodes (d = 5 mm) were used. The electrocatalysts were deposited as an ink on the surface of these electrodes. For every measurement, the ink was prepared by dispersing 24.0 mg of electrocatalyst in 900 μL of a 1 wt% solution of polystyrene in toluene. Polystyrene was chosen as binder instead of the commonly applied Nafion® because the latter would dissolve in the ethanolic reaction medium, causing the electrocatalyst to peel off from the electrode during experiments. The use of polystyrene instead of Nafion® does not alter the electrochemical behaviour, as shown in a test with a standard electrocatalyst for the oxygen reduction reaction (see Fig. S1). Approximately 3.47 μL of this ink was deposited on the glassy carbon electrode, after which toluene was evaporated at 50 °C for 20 min in an oven. For each electrocatalyst, three replicate electrodes were prepared with an average catalyst loading of 0.47 mg/cm². The counter electrode was a Pt grid and the reference electrode was a Fc⁺/Fc reference electrode (E_{Fc+}/Fc = 0.64 V vs. S.H.E.). All potentials in this paper are referred to this redox couple. The measurements for the nitrobenzene reduction reaction were carried out in a 0.3 M HClO₄ ethanolic solution, with traces of water originating from the aqueous solution. To avoid possible interference of the oxygen reduction reaction, nitrogen gas was bubbled through the electrolyte for 30 min to remove O₂ prior to the measurements. A thermostatic bath was used to control the

electrolyte temperature, which was set at 25 °C. For the linear sweep voltammetry (LSV) measurements, 50 mL of 5 mM nitrobenzene electrolyte solution was used. The potential was scanned in the range from -0.2 to -1.8 V vs. Fc⁺/Fc at a rate of 5 mV s⁻¹. Blank measurements, i.e. in the absence of nitrobenzene, were performed with each electrocatalyst before analysing the nitrobenzene reduction. Every measurement was carried out three times in order to increase the reliability of the experimental results and the average values were reported throughout the paper. The reproducibility of the electrocatalyst synthesis was also verified by testing two different batches of Cu-PANI-AC-A, which resulted in a comparable electrocatalytic performance. After each measurement, the potential was corrected for the ohmic potential drop as a consequence of the electrolyte resistance between the reference and the working electrode. By means of electrochemical impedance spectroscopy an electrolyte resistance of 125 ohm was found for the 0.3 M HClO₄ ethanolic solution.

The onset potential, i.e. the potential at which the nitrobenzene reduction reaction starts, was determined as the potential at which the slope of the LSV plot exceeded 0.1 mA cm⁻² V⁻¹. The half-wave potential, i.e. the potential at which the reaction is in the middle of the mixed kinetic-diffusion regime, was determined as the potential corresponding to the inflection point in the LSV plot. The Koutecký-Levich (K-L) equation [Eq. (1)] was used to calculate the number of exchanged electrons (n) and to determine the kinetic current density (J_K) [12].

$$\frac{1}{J} = \frac{1}{J_K} + \frac{1}{J_D} = \frac{1}{J_K} + \frac{1}{B\omega^{1/2}} \quad (1)$$

where J is the recorded current density, which can be expressed in terms of kinetic current density (J_K) and diffusion-limited current density (J_D). The latter can be also expressed as a function of the angular velocity (ω) of the rotating ring disk electrode. B and J_K are defined by Eqs. (2) and (3):

$$B = 0.62nFC_0(D_0)^{2/3}\nu^{-1/6} \quad (2)$$

$$J_K = nFkC_0 \quad (3)$$

where n is the number of exchanged electrons, F is the Faraday constant, k is the electron transfer rate constant, C₀ is the bulk concentration of nitrobenzene (5 × 10⁻⁶ mol cm⁻³), ν is the kinematic viscosity of the electrolyte (0.0152 cm² s⁻¹) and D₀ is the diffusion coefficient (4.7 × 10⁻⁶ cm² s⁻¹) [9]. At a given potential, n can be determined from the slope of the K-L plots. The kinetic current density can be determined from the intercept with the y-axis. The current densities were calculated with respect to the geometric surface area of the glassy carbon electrode disk (A_{geo}) as the actual surface area could not be calculated in an accurate manner (as it depends both on the electrocatalyst specific surface area and on the amounts of electrocatalyst and binder that are applied to the disk). This feature has to be kept in mind when comparing different values for the kinetic current density, as they will not only include contributions of the intrinsic activity per surface unit but also of the specific surface area of the electrocatalyst [7]. While this allows a meaningful ranking of the electrocatalytic performance of different materials, it should be noted that this ranking is conceptually different from comparisons where the kinetic current density is normalised with respect to the electrochemically active surface area and is thus only a function of the intrinsic activity (per surface unit).

In order to investigate the conversion and the product distribution in the nitrobenzene reduction reaction over the most promising electrocatalysts, chronoamperometric experiments were performed in a cell that was split in an anodic and a cathodic compartment by means of a Zirfon® separator [34]. The rotation speed of the working electrode was set at 500 rpm and the potential was set at -0.75 V vs Fc⁺/Fc in 0.3 M HClO₄ in ethanol. The volume at the working electrode was 170 mL and a concentration of 15 mM of nitrobenzene was used. At the end of the test (52 h), the pH of the reaction solution was adjusted to 7 in two

steps: (1) to a pH between 4 and 5 with 1 M KOH ethanolic solution and (2) to a pH of 7 with a phosphate buffer solution (pH = 7). Finally, insoluble KClO_4 was filtered out. The product concentrations were measured by GC. Each GC analysis was done in triplicate and the average results were reported. The electrochemical stability for selected electrocatalysts was determined using cyclic voltammetry (CV). The potential was cycled between -0.2 to -1.8 V vs. Fc^+/Fc at a scan rate of 100 mV s^{-1} in a 0.3 M HClO_4 electrolyte containing 5 mM nitrobenzene. 1000 cycles were performed and prior to the last scan the solution was stirred in order to homogenise the nitrobenzene concentration in the half-cell. The second and the last scan were compared to evaluate the electrocatalyst stability.

3. Results and discussion

Metal-containing N-doped carbon electrocatalysts with a different content of N and of non-noble metals (Fe, Co or Cu) were prepared by pyrolysing composite materials consisting of activated carbon, poly-aniline and incorporated metal sites (Me-PANI-AC). It is the first time that Cu was used as metal in the synthesis of Me-PANI-AC electrocatalysts, whereas the Fe- and Co-containing have already been reported as electrocatalysts for the oxygen reduction reaction and for the reduction of NO to NH_2OH [10,31]. Here, the Me-PANI-AC materials were tested for the electrocatalytic reduction of nitrobenzene, with the industrially relevant aniline as target product.

The main features of the Me-PANI-AC materials that are foreseen to define their electrocatalytic performance in the reduction reaction under investigation are (1) the metal type, loading and configuration, (2) the N loading and configuration, (3) the surface area and (4) the degree of graphitisation [12]. To correlate these physicochemical properties of the Me-PANI-AC materials with their electrocatalytic performance in the nitrobenzene reduction reaction, the materials were thoroughly characterised with a set of techniques.

3.1. Physicochemical characterisation

Up to date, almost all reported electrocatalysts for the nitrobenzene reduction reaction contain noble (e.g. Pt [7,21]) or non-noble (e.g. Cu [8,17]) metals as active site. The metal can act as a coordination site for nitrobenzene, thus promoting its reduction. In this context, it is important to investigate the influence of the metal nature and loading on the electrocatalytic performance in the reduction of nitrobenzene to aniline. For this purpose, the Me-PANI-AC electrocatalysts were prepared with different type (Fe, Co or Cu) and with different amount of metal (see Table 1). The composition of the prepared electrocatalysts (Table 1) was determined by means of TGA (overall metal content) and XPS (surface carbon, nitrogen, oxygen, sulphur and metal content).

TGA analysis shows that the final loading of metal is higher for the Me-PANI-AC-B and -C electrocatalysts, which is in line with the higher ratio of metal and aniline relative to activated carbon that was employed in their synthesis. Based on the literature, it is expected that a

significant fraction of the metals is present in a coordination with N-atoms, which originate from aniline. Therefore, a higher aniline content should allow retaining a larger amount of metal. However, for the higher metal loadings, a significant fraction of the employed metals was not incorporated in the final material. This might mean that not enough N atoms are available to bind the metal species. Furthermore, as will be demonstrated in more detail later on by means of XRD, XPS and ToFSIMS characterisation, not all metal species are coordinated to nitrogen, but also metal oxides and sulphides are present. It is expected that these species have a weak interaction with the carbon framework and, therefore, can be largely removed from the surface of the materials by the applied acid treatment (see 2.2 in the Experimental section). This explains the lower metal loadings that were detected by XPS (Table 1), which is a surface-sensitive technique (analysis depth up to a few nm). For the higher metal loadings, one acid treatment is not sufficient to remove all unstable metal species and the metal content tends to decrease further after a second acid treatment. Differences in the surface metal contents can significantly affect the electrocatalytic performance (*vide infra*). In the Fe- and Cu-containing materials, also the N/C ratio is higher for the series B and C materials, as anticipated based on the higher N content in the synthesis mixture. An opposite behaviour was observed for the Co-containing materials, as the N/C ratio was lower in the electrocatalysts prepared with a higher aniline content. This trend can be explained by considering the standard reduction potentials (E°) of the different metal ions present during the polymerisation of aniline: E° decreases from Fe^{3+} ($0.77 \text{ V}_{\text{SHE}}$) to Cu^{2+} ($0.34 \text{ V}_{\text{SHE}}$) to Co^{2+} ($-0.28 \text{ V}_{\text{SHE}}$), which means that copper and particularly iron can act more readily as an oxidant. Thus, iron(III) and copper(II) chloride are expected to promote the aniline polymerisation, while cobalt(II) chloride rather works as an inhibitor. This would explain why the increase in the N/C ratio with the metal content is the largest for iron and also why the N/C ratio decreases for the materials prepared with higher initial cobalt content (Table 1).

XRD was used to investigate the presence of crystalline phases in the different Me-PANI-ACs. For the Me-PANI-AC-A samples, the diffractograms only displayed two broad peaks around $2\theta = 26$ and 44° (Fig. S2), which are characteristic for the (002) and (101) graphitic planes with a rather low degree of crystallinity [12,35]. On the other hand, the diffractograms of the materials prepared with higher metal loadings (Me-PANI-AC-B and -C) display peaks ascribed to several different crystalline phases (Fig. 1). For the Fe- and Co-PANI-AC materials, the observed XRD peaks can be ascribed to metal sulphides (FeS and Co_9S_8 , respectively). Co-PANI-AC-B and -C probably also contain small amounts of metallic cobalt, as suggested by the low intensity peak marked with (*) in Fig. 1, which corresponds to the (111) plane of Co in the face-centred cubic system. The presence of metal sulphides is in agreement with the XPS results, which show higher S content for the Fe- and Co-containing electrocatalysts that were prepared with higher metal loadings. Furthermore, it was observed that even after a second acid treatment, these peaks (although less pronounced) remain detectable, which most likely means that these remaining sulphides are

Table 1

Specific surface area (determined from the N_2 physisorption data) and elemental composition of the Me-PANI-AC materials (with Me = Fe, Co or Cu).

	S_{BET} (m^2/g)	Metal (wt%)		N (wt%)		C (wt%)		O (wt%, from XPS)	S (wt%, from XPS)
		Theor.	Total (TGA)	Surface (XPS)	Theor.	Surface (XPS)	Theor.		
Fe-PANI-AC-A	489	4.2	4.6	1.9	4.2	4.5	90	88	5.6
Fe-PANI-AC-B	196	33	18	3.8	8.4	10	54	80	4.7
Fe-PANI-AC-C	358	33	16	2.4	8.4	7.6	54	83	4.9
Co-PANI-AC-A	539	4.4	8.1	1.2	4.2	4.0	89	90	4.1
Co-PANI-AC-B	108	40	38	4.4	7.6	3.3	49	76	10
Co-PANI-AC-C	342	40	18	4.5	7.6	2.1	49	81	6.2
Cu-PANI-AC-A	533	4.7	3.9	1.0	4.1	5.8	89	88	5.0
Cu-PANI-AC-B	120	36	27	6.1	8.0	8.8	52	75	9.4
Cu-PANI-AC-C	373	36	17	4.5	8.0	6.1	52	73	16

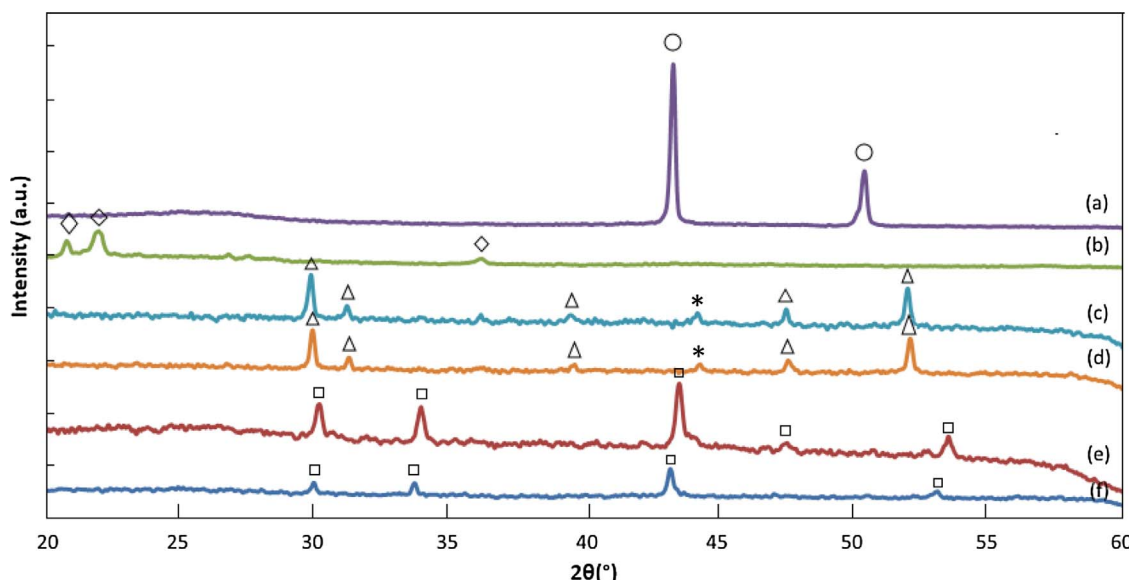


Fig 1. X-ray diffractograms of: (a) Cu-PANI-AC-B, (b) Cu-PANI-AC-C, (c) Co-PANI-AC-B, (d) Co-PANI-AC-C, (e) Fe-PANI-AC-B and (f) Fe-PANI-AC-C. The peaks in the XRD pattern are identified as follows: \circ is metallic copper, \diamond is SiO_2 , $*$ is metallic cobalt, Δ is Co_9S_8 and \square is FeS .

covered by several carbon layers, impeding their removal. The origin of the metal sulphides can be found in the degradation of the ammonium peroxydisulphate (APS) used to promote the formation of polyaniline. The absence of sulphides in Fe- and Co-PANI-AC-A is ascribed to the lower APS/metal ratio and to the higher aniline/metal ratio that were used in the synthesis of these samples. The latter can promote the coordination of the metal with N atoms, which has been shown by ToF-SIMS to occur mainly as MeN_2 or MeN_4 species and, thus, to be favoured by a higher N content relative to the metal [36,37]. In the case of the Cu-PANI-AC materials, no sulphides could be detected at higher metal loadings, in agreement with the lower S content detected by XPS (see Table 1). The peaks for Cu-PANI-AC-B are ascribed to metallic copper (\circ in Fig. 1). After a second acid treatment the metallic copper species appear to be completely removed and the observed peaks are ascribed to SiO_2 impurities (Δ in Fig. 1), originating from the quartz wool used during the pyrolysis.

The surface area of the Me-PANI-AC electrocatalysts was determined by N_2 -physisorption (Table 1). Two trends can be observed: (1) the surface area tends to decrease with higher (theoretical) metal and nitrogen content because a larger fraction of non-porous metal species (oxides or sulphides) are produced and (2) a second acid treatment partially restores the surface area by further removing the unstable metal species, generating additional porosity.

Useful information on the degree of graphitisation and on the defectivity of the synthesised electrocatalysts can be obtained with Raman spectroscopy (Table 2 and Fig. 2). The presence of graphitic structures in the Me-PANI-AC materials is evidenced by the presence of the G-band at $1590\text{--}1600\text{ cm}^{-1}$, which stems from the E_{2g} in-plane vibration of the graphitic carbon framework and, therefore, is assigned to the planar vibration of sp^2 C atoms in an ideal graphitic plane [12]. Due to the change in the electronic structure of the carbon lattice caused by the presence of the electron-donating N atoms, the peak is shifted to lower wavenumbers compared to pure undoped carbons [38]. The other main signal at approximately 1350 cm^{-1} (D-band) is associated with defects at the edges of the sp^2 domain. Two additional peaks, centred at 1200 and 1500 cm^{-1} (A-band), can be identified upon deconvolution of the Raman spectra (Fig. 2). These are generally attributed to C atoms outside the perfectly planar graphitic framework and to heteroatoms inside the graphite lattice, respectively [35]. The relative degree of graphitisation can be estimated through a set of 3 parameters (Table 2): (1) the ratio of the areas of the D and G bands ($A_{\text{D}}/A_{\text{G}}$), which is inversely proportional to the degree of graphitisation, (2) the full-width-

half-maximum (FWHM) of the D-band and (3) the area of the A-band, a higher value of the latter two being generally correlated with a higher disorder [10,12,32]. Based on these parameters, it was determined that at low metal loadings (i.e. in Me-PANI-AC-A) the highest degree of graphitisation was obtained in the material containing iron, followed by cobalt and copper. This is in accordance with literature reports, in which iron was identified as a good catalyst for promoting graphitisation, followed by cobalt. Copper was found to be less efficient in promoting the graphitisation reaction, since it is unable to form metal carbides [39–42]. An increase in the metal content used in the preparation of the materials led to higher degree of graphitisation in the case of Co-PANI-AC materials, but to a lower one in the case of the Fe and Cu counterparts (Table 2). The trend observed in the iron- and copper-containing composites is ascribed to the higher incorporation of N when the materials are prepared with higher metal content (*vide supra*): the higher fraction of N-containing PANI compared to that of activated carbon in the composite material can account for the observed lower degree of graphitisation [12]. The trend observed in the cobalt-containing material can be correlated to the above-mentioned activity of cobalt in promoting the carbonisation process, together with the observed lower incorporation of N at higher Co content (*vide supra*). The latter feature is what distinguishes Fe from Co and thus seems to be the main factor determining the trend in graphitisation degree as a function of metal loading. A final trend that was observed is that the degree of graphitisation decreases after a second acid treatment, which is a consequence of the removal of both metal species and N atoms from the carbon framework, leaving behind extra defects that are not fully repaired by the second pyrolysis step.

Further insight in the configuration of the metals and of the N, O and S atoms in the Me-PANI-AC materials was obtained by deconvolution of the high-resolution XPS signals. The deconvolution of the N 1s XPS signal allows quantifying the different N configurations that are typically present in a N-doped sp^2 carbon lattice (Fig. 3 and Table 2): pyridinic N (N1, at a binding energy between $398.0\text{--}399.3\text{ eV}$); pyrrolic N (N2, at $399.8\text{--}401.2\text{ eV}$); graphitic N (N3 and N4, at $401.1\text{--}402.7\text{ eV}$) and oxidised pyridinic N (N5, $> 402.8\text{ eV}$) [12,31,32]. The difference between N3 and N4 is the location of the graphitic N in the carbon framework: N3 is found at the edges of the sp^2 carbon framework, while N4 is located in the bulk of the framework. Since transition metals like iron, cobalt and copper can bind with N (e.g. like in a phthalocyanine or porphyrin complex), two other N configurations, where N is bound with the metal (Fig. 3), can be present in the Me-PANI-AC materials. Since

Table 2
N configuration and percentage of surface metal oxides present in the Me-PANI-AC materials as determined with XPS and summary of parameters related with degree of graphitisation as determined by Raman.

Sample	Pyridinic N (or N-Fe) ^a	Pyrrolic N ^a	Graphitic N ^a	Oxidised pyridinic N ^a	N _{pyr} /N _{graph} ^a	% Metal in oxides ^b	% Metal in sulphides ^c	A _D /A _G ^d	FWHM D-band ^d	Area% of A-band ^d
Fe-PANI-AC-A	40	15	41	5	1.0	13	/	1.0	11	147
Fe-PANI-AC-B	40	4	45	11	0.9	17	1.1	1.1	21	152
Fe-PANI-AC-C	42	1	49	7	0.9	38	6.5	1.2	23	155
Co-PANI-AC-A	41	11	40	8	1.0	37	/	1.1	17	149
Co-PANI-AC-B	26	7	53	14	0.5	66	26	0.9	16	136
Co-PANI-AC-C	41	0	45	14	0.9	28	27	1.0	17	145
Cu-PANI-AC-A	45	6	43	6	1.0	100	/	1.3	27	156
Cu-PANI-AC-B	39	10	47	3	0.8	100	/	1.3	30	169
Cu-PANI-AC-C	43	0	48	10	0.9	100	/	1.4	30	172

^a As determined by deconvolution of the high resolution N 1s XPS signals with MultiPak.

^b Calculated based on the metal and oxygen contents at the surface and on the percentage of oxygen that is in a metal oxide (or hydroxide) configuration. The latter was determined by deconvoluting the O 1s XPS signals with MultiPak.

^c Calculated based on the metal and sulphur contents at the surface and on the percentage of sulphur that is in a metal sulphide configuration. The latter was determined by deconvoluting the S 2p XPS signals with MultiPak [17]. The symbol / indicates that too low sulphur content was present in the sample resulting in too low signal-to-noise ratio, hence making it impossible to deconvolute the signal.

^d As derived from the deconvolution of the Raman spectra, which was performed with the IgorPro software.

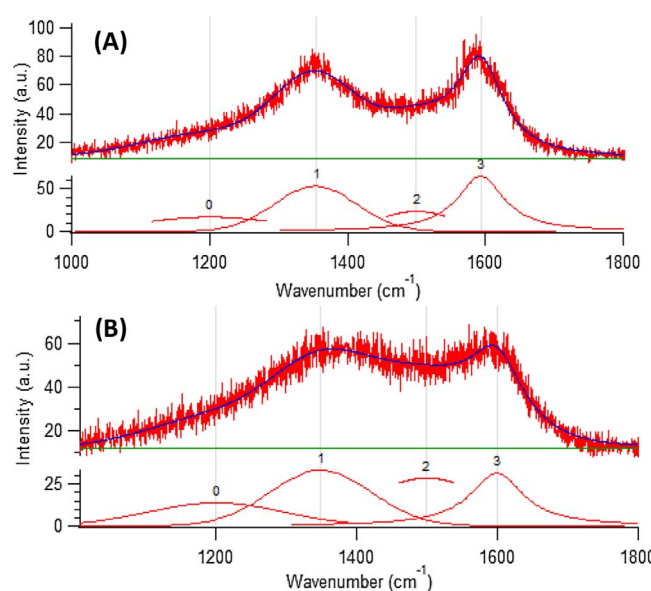


Fig. 2. Deconvoluted Raman spectra of Co-PANI-AC-B (A) and Cu-PANI-AC-B (B).

these N-Me species give a signal at around 399.2 eV, they cannot be distinguished from the pyridinic N configuration [32].

When comparing the N configurations for the different metal species, it is observed that the graphitic and the pyridinic N configurations form the largest fraction in all cases. Combining the data in Table 1 and 2, it can also be concluded that the N configuration is influenced by the relative amount of metal employed in the synthesis of the Me-PANI-ACs. The materials prepared with higher metal content (series B and C) display a higher ratio of graphitic to pyridinic and pyrrolic N atoms (see also Figs. 3 and S3). This may be explained by the above-mentioned role played by the metal in promoting the graphitisation process. This does not imply a higher degree of graphitisation, as was shown above for Fe- and Cu-PANI-AC, because a higher fraction of N atoms is incorporated in the material. The fact that the pyridinic N fraction, which also includes the N-Me configuration, does not increase with increasing metal content also suggests that insufficient N atoms for coordinating the metals are available and, therefore, other metal species (sulphides and oxides) are formed. The presence of oxides or hydroxides, although not detected by XRD (thus pointing to their amorphous nature), is confirmed by a contribution assigned to metal bound to oxygen (± 530 eV) in the deconvoluted O 1s XPS signals (Figs. S4–6). The percentage of surface metal species that is present in the form of oxides and/or hydroxides can be calculated based on the results of the deconvoluted O 1s XPS signals and on the surface oxygen and metal contents (Table 2). Since the resolution in the O 1s signals does not allow distinguishing between oxides and hydroxides, in our calculations it was assumed that the Fe-O signal stems from Fe_2O_3 , the Cu-O signal from CuO and the Co-O from CoO. Based on these estimates, a significant fraction of the metals at the surface of the Me-PANI-ACs is present in the form of oxides/hydroxides (Table 2). In the case of the Cu-PANI-AC, such species account for the totality of the metal content. The reason behind this different tendency of each metal to form oxides/hydroxides rather than metal-N bonds is most likely related to the Me-N bond strength. By means of density functional theory studies, it has been determined that the Me-N bond strength decreases in the order $\text{Fe-N} \approx \text{Co-N} > \text{Cu-N}$ for porphyrins [43], phthalocyanines [43] and in N-doped carbon nanotubes [44]. It is also worth noting that the iron and copper oxides/hydroxides are strongly anchored to the composite material, as shown by the fact that they do not get removed during the acid treatment, whereas in the case of Co-PANI-ACs a major drop in the content of oxides/hydroxides is observed upon treatment with H_2SO_4 (compare series B and C in Table 2). Following a similar approach, the

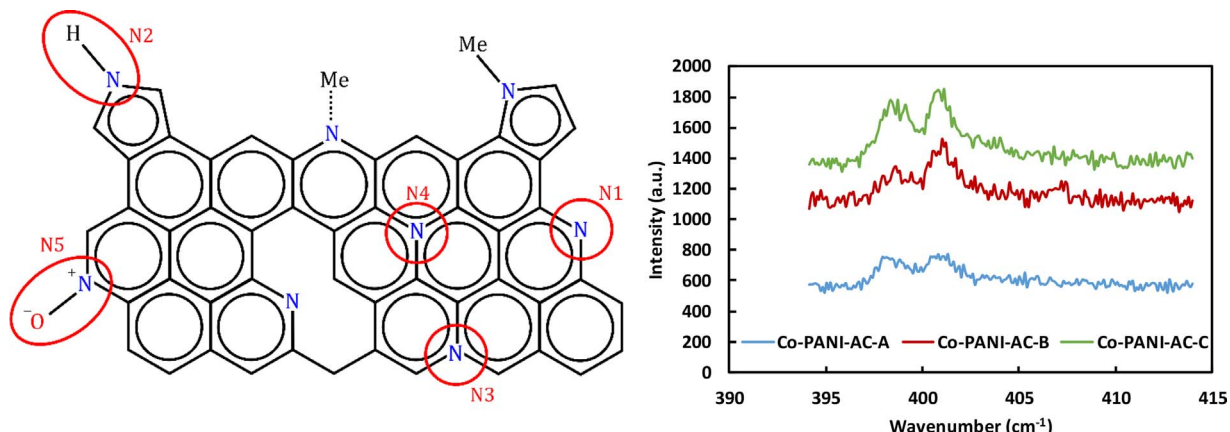


Fig. 3. Left: illustration of the different possible N configurations inside a graphitic carbon lattice. Right: N 1s XPS signal of Co-PANI-AC-A, -B and -C.

percentage of surface metal species that is present in the form of sulphides was also calculated (Table 2). In agreement with the XRD results, it was found that a significant fraction of the metals at the surface of Fe-PANI-AC-B and -C and of Co-PANI-AC-B and -C is made up of sulphides. To further evaluate the configuration of the metals inside the Me-PANI-AC materials, the high resolution XPS 2p signals of the three metals were investigated for the B and C series, i.e. those with higher metal loadings (Figs. 4 and S7).

For Cu-PANI-ACs, the high resolution Cu 2p_{3/2} signal can be deconvoluted into three peaks at 932.4 eV (Cu₂O or Cu), 933.7 eV (CuO) and 935.0 eV (Cu(OH)₂ or Cu-N complexes) [45,46]. The satellite peaks (not visible) at 942.4 eV would indicate the presence of Cu(II) species as main fraction [47]. Cu-PANI-AC-B contains metallic Cu (XRD), though this is likely to be covered with an oxide/hydroxide layer [7,8], which might be the only species accounting for the signal at 932.4 eV as XPS is a surface-sensitive technique. The other two peaks are assigned to CuO and Cu(OH)₂ based on the deconvolution of the O 1s XPS signal (Fig. S5), though the presence of small amounts of Cu-N cannot be excluded. For Co-PANI-ACs, the Co 2p_{3/2} signal was deconvoluted in three peaks at around 778, 781 and 785 eV, which are respectively assigned to Co (0)/Co(I) [48–54], Co(II)/Co(III) [54–56] and a satellite peak ascribed to the presence of cobalt oxides [57,58]. These assignments are supported by the XRD characterisation (for Co₃S₈ and Co) and by the deconvolution of the O 1s XPS signal (for the oxides; see Figs. S4–6).

In the high resolution Fe 2p XPS signal, two main bands can be visualised at around 711 and 723 eV, originating from 2p_{3/2} and 2p_{1/2} photoelectrons, respectively. Based on the literature, the signal was deconvoluted in five peaks (Figs. 4 and S7): 709.2 (Fe(II) 2p_{3/2}), 711.3 (Fe(III) 2p_{3/2}), 716.8 (satellite peak confirming the presence of Fe(III)), 722.3 (Fe(II) 2p_{1/2}) and 725.1 eV (Fe(III) 2p_{1/2}) [45,59–66]. These data, in combination with those presented above (XRD; O 1s and N 1s signals in XPS), suggest the presence of various types of iron oxides (FeO, Fe₃O₄, Fe₂O₃), of iron sulphides and, likely, of FeN_x species. When the deconvolution of the Me-PANI-AC-B and -C series are compared with each other (Figs. 4 and S), it is observed that for the Cu-containing materials the configuration remains rather similar, while for Co- and Fe-containing materials some important differences could be distinguished. In the material that underwent a second acid treatment (Co-PANI-AC-C), the fraction of cobalt in the lowest oxidation states [Co(I)/Co(0)] decreased compared to that of cobalt in higher oxidation states [Co(III)/Co(II)]. In the case of the Fe-PANI-ACs, the second acid treatment led to a decrease of the Fe(III) fraction relative to the Fe(II) fraction. These changes might have important implications for the electrochemical performance, as will be discussed in Section 3.2.

For the Me-PANI-AC materials with lower metal loadings (i.e. series A), the nature of the different metals was investigated by Time of Flight-Secondary Ion Mass Spectroscopy (ToF-SIMS). Only the positive secondary ions were taken into account here, since the signal for Cu-

PANI-AC-A in the negative mode was much weaker. This analysis revealed that Fe- and Co-PANI-AC-A contain the anticipated MeN_xC_y species, where y is in the range from 0 to 12 (larger compounds could no longer be distinguished from the background signal) and x is in the range from 1 to 4 (see Table 3) [36,37]. On the other hand, no MeN_xC_y species were observed in Cu-PANI-AC-A. These results are in accordance with the XPS results. Particularly, it is worth noting that the fraction of metal in the form of oxides follows the same trend with both techniques, being the lowest for Fe-PANI-AC-A, followed by Co-PANI-AC-A and finally by Cu-PANI-AC-A, in which Cu results to be present exclusively as copper oxide (see Table 2 and the last column of Table 3). Although the trend is clear, it should be kept in mind that the relative amounts of the different types of metal sites determined by XPS and ToF-SIMS should be considered only as a qualitative estimate. Finally, ToF-SIMS also confirms the absence of metal sulphides in the Me-PANI-AC-A materials, in agreement with the XRD results.

TEM and STEM were used to analyse the size of the metal particles present in the different Me-PANI-AC materials. The STEM-analysis was coupled to EDX mapping, which allowed monitoring the composition of the samples, with special attention to the crystalline particles. The size and the nature of the metal-containing particles present in the various materials is expected to have an important impact on the electrocatalytic activity of the different materials. These aspects will be discussed in Section 3.2. For the materials from series A, no (crystalline) particles could be observed (Figs. S8, S11 and S14), in line with the absence of diffraction peaks related to metal-containing species in the XRD patterns of these materials. This result, in combination with the ToF-SIMS and XPS data, suggests that the metal species inside the Me-PANI-AC-A materials are present as isolated sites (MeN_xC_y species) or organised in amorphous domains. On the other hand, for the materials with higher metal loadings (series B and C), crystalline particles of 10–20 nm could be generally distinguished in the TEM images (Figs. S8, S11 and S14). EDX mapping was used to determine the composition of these particles. For Cu-PANI-AC-B, the particles consisted of metallic copper and/or copper oxide, whereas only large particles consisting mainly of silica with minor fractions of copper oxide were found in Cu-PANI-AC-C (Figs. S9 and S10). The particles in Cu-PANI-AC-B are assigned to metallic copper (this phase was identified by XRD in Cu-PANI-AC-B, see Fig. 1), covered by a layer of copper oxides/hydroxides (which were identified by XPS) [7,8]. The crystalline particles in Co-PANI-AC-B and -C are identified as cobalt sulphides by EDX mapping (Figs. S12 and S13), in accordance with the XRD results (Fig. 1). Finally, Fe-PANI-AC-B contains rather large, mainly amorphous, iron oxide particles (Fig. S15), whereas no metal-containing particles could be distinguished in Fe-PANI-AC-C (Fig. S16). No iron sulphides were detected in the areas analysed by EDX, though the presence of these species in Fe-PANI-AC-B and -C was proven by XRD. This suggests a non-homogeneous distribution of the sulphides within the materials.

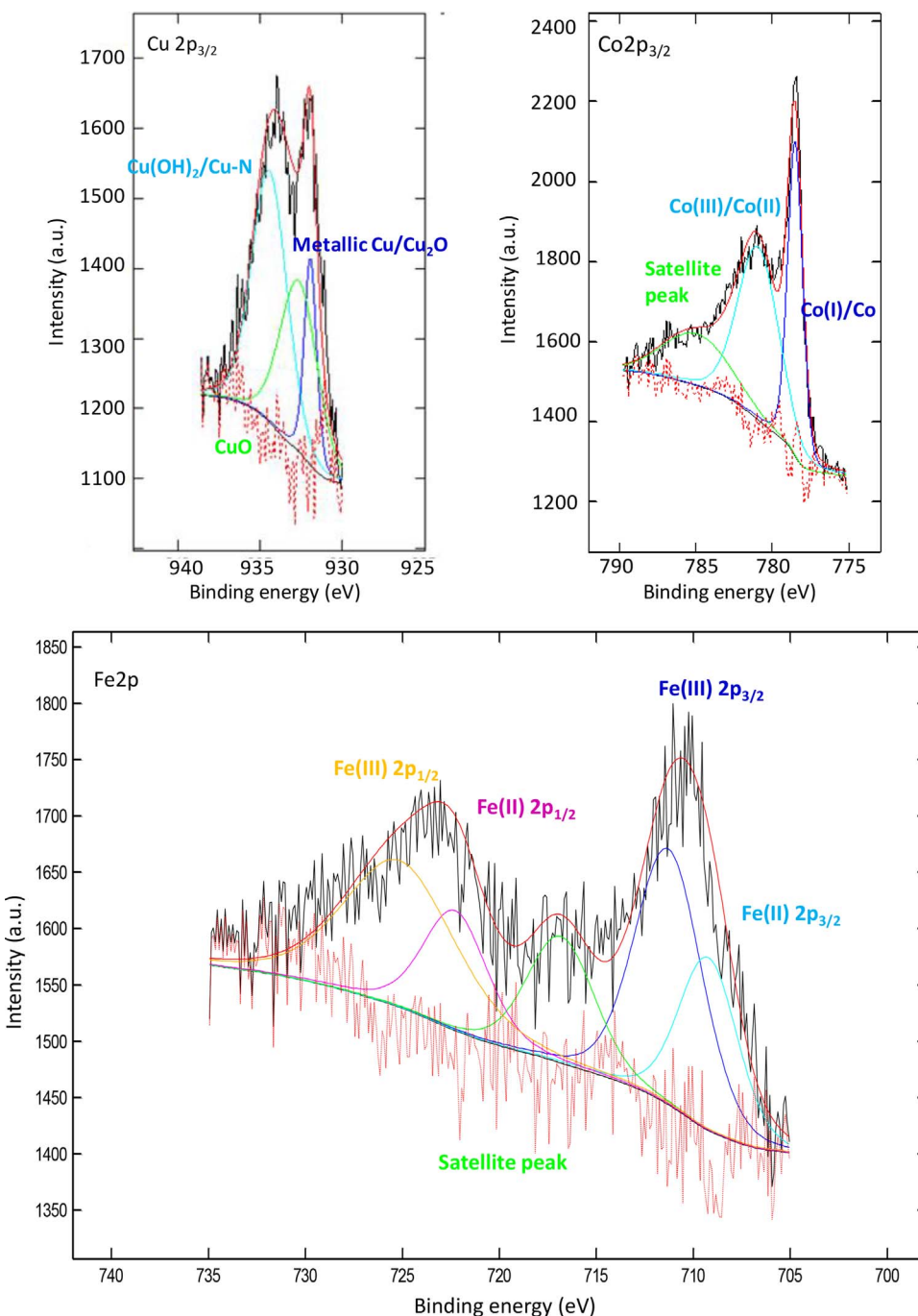


Fig. 4. Deconvoluted high resolution Me 2p XPS signals of the Me-PANI-AC-B series.

Table 3

Relative abundance of MeN_xC_y^+ ions (in %) for Cu-, Co- and Fe-PANI-AC-A, as determined by analysis of the positive secondary ions by ToF-SIMS.

	MeNC_y^+	MeN_2C_y^+	MeN_3C_y^+	MeN_4C_y^+	$\frac{\text{MeN}_x\text{C}_y^+}{\text{Me}_2\text{Ou}}$
Fe-PANI-AC-A	53	19	16	12	0.36
Co-PANI-AC-A	27	24	23	25	0.13
Cu-PANI-AC-A	0	0	0	0	≈ 0

In summary, the physicochemical characterisation highlighted several features of the Me-PANI-AC-A materials: (1) the metal type has an important influence on the resulting metal configuration, with iron and cobalt being able to form MeN_x species whereas copper forms preferentially metallic copper and copper oxide species; (2) the materials

prepared with higher metal and aniline loadings in the synthesis mixture display a higher metal loading; (3) a single acid treatment proved to be insufficient to remove all unstable metal species.

3.2. Electrocatalytic reduction of nitrobenzene

3.2.1. LSV measurements and Koutecký-Levich analysis

The performance of the different Me-PANI-ACs as electrocatalysts for the cogeneration of electricity and aniline was first evaluated by means of linear sweep voltammetry (LSV) in a half-cell setup (Figs. 5 and S17–S25). LSV is a suitable technique for the investigation of complex redox reactions as the nitrobenzene reduction reaction [7,9,21]. The activity of the electrocatalysts can be ranked based on the onset potential, the half-wave potential and the current generation in the potential range of interest for the aniline production (i.e. -0.7 to

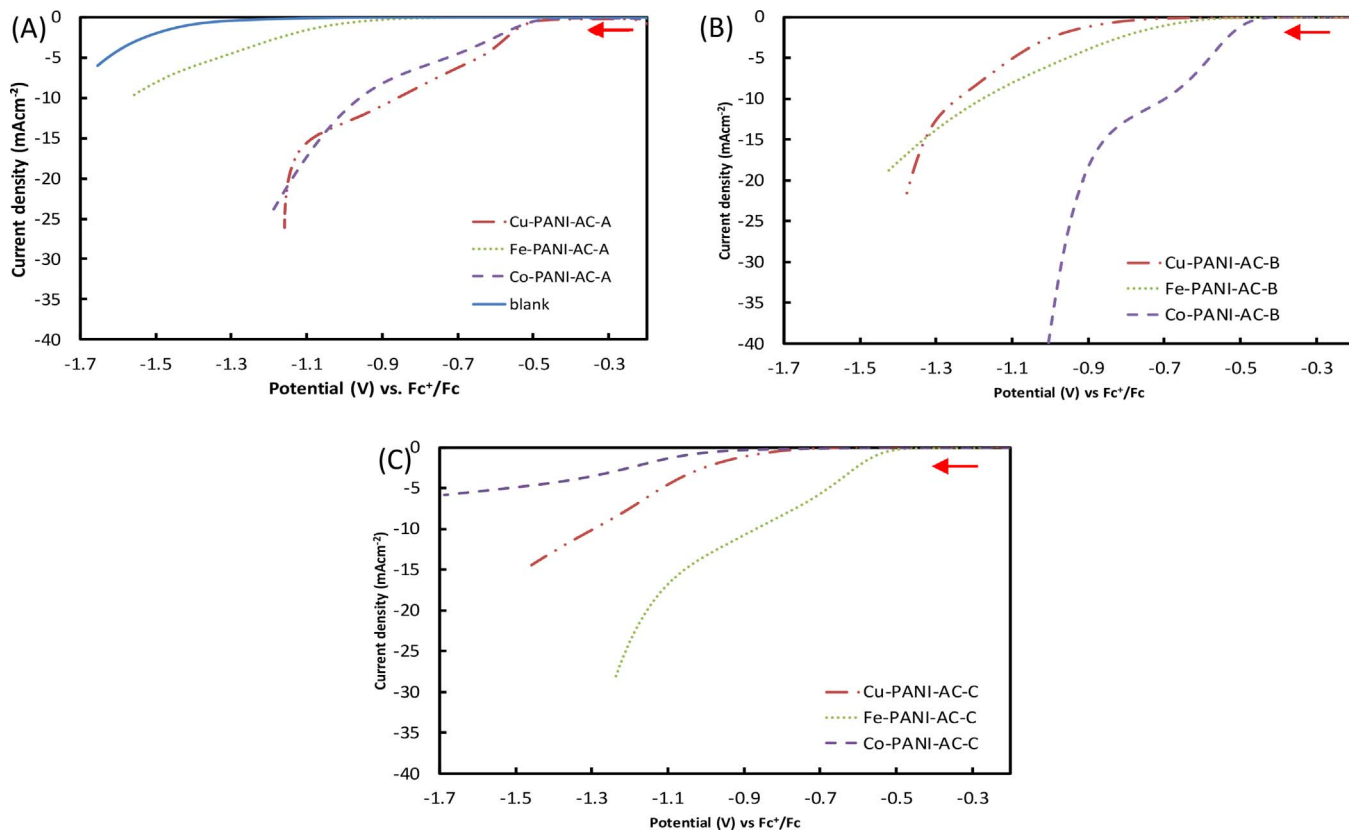


Fig. 5. LSV plots of (A) Me-PANI-AC-A, (B) Me-PANI-AC-B and (C) Me-PANI-AC-C, recorded in 5 mM nitrobenzene in 0.3 M HClO_4 in ethanol at a scan rate of 5 mV s^{-1} , with a rotation speed of 2000 rpm and corrected for the iR drop. The LSV tests were carried out by varying the potential of the working electrode from -0.2 to -1.8 V vs. Fc^+/Fc at four rotation speeds (500, 1000, 1500 and 2000 rpm, Figs. S17–S25).

Table 4

Summary of nitrobenzene reduction parameters derived from the linear sweep voltammetry results. Average values and standard deviations are reported for n and J_K . For the onset and the half-wave potential the average values are reported (the standard deviation is between 0.005 and 0.01 V).

Electrocatalyst	n @ -0.75 V	J_K @ -0.75 V (mA cm^{-2})	Onset potential (V)	Half-wave potential (V)
Fe-PANI-AC-A	4.2 ± 0.1	-0.1 ± 0.1	-0.58	-1.27
Fe-PANI-AC-B	/	/	-0.37	-0.90
Fe-PANI-AC-C	8.9 ± 0.5	-8.6 ± 0.4	-0.33	-0.73
Co-PANI-AC-A	5.4 ± 0.2	-9.1 ± 0.3	-0.27	-0.67
Co-PANI-AC-B	9.2 ± 0.5	-20 ± 1.0	-0.30	-0.64
Co-PANI-AC-C	/	/	-0.50	-1.18
Cu-PANI-AC-A	5.8 ± 0.2	-15 ± 0.6	-0.28	-0.64
Cu-PANI-AC-B	/	/	-0.52	-1.16
Cu-PANI-AC-C	/	/	-0.53	-1.17
PANI-AC-A	2.4 ± 0.2	-2.8 ± 0.1	-0.45	-0.98

-0.9 V) – see Table 4 and Fig. 5. In order to initiate the reaction with high rate, the electrocatalyst should promote the first electron transfer, which is accompanied by the adsorption of nitrobenzene, at high rate. This would correspond to a low overpotential (i.e. the difference in potential between the onset potential and the standard reduction potential of the reaction in question). Further information on the activity and an estimate of the selectivity are provided by the Koutecký-Levich plots (Figs. 6 and S27–S29), which were constructed on the basis of the results of the LSV experiments performed at different rotation speeds of the working electrode. By comparing the LSV curves for the three series of Me-PANI-AC materials, it was observed that the metal leading to the best performing electrocatalyst differs for each series (Fig. 5). Among the materials with the lowest metal loading (series A), the Cu-based electrocatalyst gave the highest current densities, followed closely by

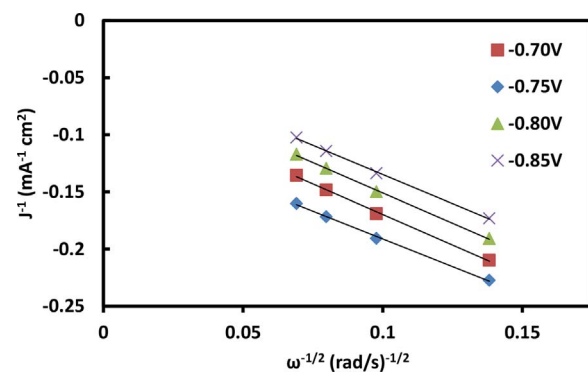


Fig. 6. Koutecký-Levich plots (J^{-1} vs. $\omega^{-1/2}$) at different electrode potentials for Cu-PANI-AC-A.

the Co-PANI-AC-A, whereas rather low current densities were observed with Fe-PANI-AC-A (Fig. 5A). A similar trend was found when considering the onset potentials and the half-wave potentials (Table 4), with very similar values for Cu- and Co-PANI-AC-A, and much more negative potentials (i.e. much higher overpotential and thus higher reaction activation energy) for Fe-PANI-AC-A. When considering series B, the Co-based electrocatalyst performed significantly better than Fe- and Cu-PANI-AC-B, both in terms of current densities (Fig. 5B) and of onset and half-wave potentials (Table 4). Finally, for series C the Fe-based electrocatalyst achieved markedly better results than the Cu- and Co-counterparts both for what concerns the current densities (Fig. 5C) and the onset and half-wave potentials (Table 4). The lack of a common activity trend in the three series of electrocatalysts reflects the complexity of the multi-step reduction of nitrobenzene (Scheme 1) and the diversity of the physicochemical features of the Me-PANI-AC materials (see Section 3.1).

The analysis of the electrocatalytic behaviour of the Me-PANI-AC materials was continued by estimating the kinetic current density (J_K) and the average number of exchanged electrons (n) by means of the Koutecký-Levich (K-L) equation (see Experimental section for more details). The number of exchanged electrons is a measure of the selectivity of the electrocatalyst. Since the reduction of nitrobenzene to aniline involves the exchange of 6 electrons (Scheme 1), the closer the n value is to 6, the more selectively aniline should be produced. However, as the plateau of the LSV curves is not well pronounced, it is likely that multiple compounds are produced at the same time. This would mean that n represents an average value for the different products. At a certain potential, n can be determined from the slope of the K-L plots. The kinetic current density, which is a measure of the activity, can be determined from the intercept.

The similarity of the slopes of the generated K-L plots (Figs. 6 and S27–S29) in the potential range from -0.70 to -0.85 V vs. Fc^+/Fc , indicates that the number of transferred electrons remains rather constant in the selected potential window (i.e. in the mixed kinetic-diffusion regime). For Cu-PANI-AC-A, the slope corresponds to a value of n very close to 6, which suggests that the 6-electron reduction process of nitrobenzene to aniline is taking place selectively over this electrocatalyst. The values for n for the other electrocatalysts and the kinetic current densities were determined at -0.75 V vs. Fc^+/Fc and are summarised in Table 4. For the electrocatalyst prepared with lower metal loading, the n value decreased from Cu-PANI-AC-A ($n = 5.8$) to Co-PANI-AC-A ($n = 5.4$) to Fe-PANI-AC-A ($n = 4.2$). Among the materials prepared with higher metal loading, only Co-PANI-AC-B and Fe-PANI-AC-C tend to reduce nitrobenzene, although the n value is close to 9 in both cases (Table 4), which is a strong indication that part of the produced aniline is further reduced to cyclohexylamine (the complete reduction from nitrobenzene to cyclohexylamine corresponds to $n = 12$). For the remaining electrocatalysts of series B and C, the limiting current density at -0.75 V vs. Fc^+/Fc did not vary with the rotation rate (Figs. S17, S22, S24, S25). Therefore, no n value can be calculated for these electrocatalysts, which are thus not active in the nitrobenzene reduction reaction. The observed, small, current generation is most likely the consequence of the reduction of ethanol (which is the solvent used for the electrolyte and whose concentration at the electrode is thus independent from the rotation rate). A control electrocatalyst prepared without any metals (PANI-AC-A, see Table 4 and Fig. S26) resulted in a significantly lower n value (2.4), which means that for the specific class of materials studied in this work, the incorporation of a metal is crucial to allow the multi-step reduction to aniline. On the other hand, the fact that a current was generated indicates that even in the absence of metals there exist sites in the material that are active in promoting the reduction of nitrobenzene. These active sites are most likely related to the presence of partially positively charged carbon atoms generated by the N-doping in the carbon material [12,67,68].

It should be noted that the electrocatalysts that gave the highest n values are also those that displayed the best performance in terms of kinetic current density (J_K), as determined using the K-L plots, and also in terms of onset and half-wave potential (Table 4).

When the average number of transferred electrons with Cu-PANI-AC-A is compared with similar non-noble metal-containing electrocatalysts in the literature (e.g. $\text{Cu}/\text{Cu}_x\text{O}$ supported on MWCNTs or on activated carbon), the selectivity towards aniline is greatly improved with the catalyst reported here ($n \approx 6$ vs. $n \approx 4$ in the literature reports) [7,8]. This proves the benefits of the applied synthesis method for the synthesis of Cu-containing electrocatalysts for the nitrobenzene reduction reaction.

The results of the electrochemical experiments can be rationalised based on the physicochemical characterisation of the electrocatalysts (see Section 3.1). First of all, it appears that the activity of the electrocatalysts is strongly related with the fraction of metal oxides present at the surface of the electrocatalysts. Indeed, for the A-series the activity

decreases from Cu to Co to Fe, which is in accordance with the decrease in metal oxides content from 100% to 13%. Furthermore, for the different Co- and Fe-containing electrocatalysts this same trend can be observed: Co-PANI-AC-B and Fe-PANI-AC-C have the highest fraction of oxides and also the highest activity (see Tables 2 and 4). However, Cu-PANI-AC-B and -C show very poor activity though virtually all the metal on their surface is in the form of copper oxides (Table 2). The marked difference in activity between Cu-PANI-AC-A and -B can be ascribed to the degree of dispersion of the copper species. The TEM analysis in combination with the ToF-SIMS, XPS and XRD data indicate that the copper oxide species are organised in small, amorphous domains in Cu-PANI-AC-A, whereas large, crystalline $\text{Cu}/\text{Cu}_x\text{O}$ particles are present in Cu-PANI-AC-B. It can be inferred that a higher degree of dispersion of copper species leads to a higher number of catalytic sites for promoting the electrochemical reduction of nitrobenzene. The hypothesis that smaller oxide domains lead to higher activity would also explain the better performance of Cu-PANI-AC-A when compared to the state-of-the-art electrocatalysts consisting of $\text{Cu}/\text{Cu}_x\text{O}$ supported on MWCNTs or on activated carbon, as in the latter the particles could clearly be distinguished in the TEM images, while this is not the case for Cu-PANI-AC-A [7]. On the other hand, the poor activity of Cu-PANI-AC-C is also attributed to the large fraction of non-conductive and non-active silicon oxides that are present in the sample. An additional cause of the low activity of Cu-PANI-AC-C is that the oxides present in these materials are covered by a layer of carbon [69], as evidenced by TEM (Fig. S8). This carbon layer might prevent nitrobenzene to reach the active species.

A second observation is that the sulphides can be excluded as active sites since Co-PANI-AC-B and -C have a similar sulphur content and a similar fraction of cobalt in the form of sulphides, but only Co-PANI-AC-B is active in the reduction of nitrobenzene. The difference in activity between the two is attributed to the removal of the active cobalt oxides responsible for the activity of Co-PANI-AC-B upon the second acid treatment carried out in the synthesis of the materials in series C, as indicated by the deconvolution of the O 1s XPS signal and by EDX mapping. This treatment also caused an increase of the fraction of cobalt in higher oxidation state, as shown by the deconvolution of the Co 2p XPS signal. Contrarily to what observed for the Co-PANI-AC materials, with the Fe-PANI-ACs the second acid treatment led to a significant improvement of the electrocatalytic behaviour (Table 4). Based on the (S)TEM, EDX and XPS characterisation data, we attribute the increased activity to a change in surface composition. After the second acid treatment, the fraction of surface iron as Fe(II) (e.g. in FeO) increased relative to Fe(III) (e.g. as Fe_2O_3) and the size of the iron oxide domains became smaller. These results suggest that well-dispersed, accessible metal sites in a (partially) reduced state are contributing to the electrocatalytic activity in the reduction of nitrobenzene. Besides the nature and amount of metal species, other features of the Me-PANI-AC materials are expected to contribute to the activity: the N content and configuration (Tables 1 and 2), the surface area (Table 1) and the degree of graphitisation (Table 2). However, no clear correlation could be found between these features and the observed electrocatalytic behaviour. Therefore, we infer that the contribution of these factors has a smaller impact on the performance of the Me-PANI-AC electrocatalysts compared to the role of the metal species.

3.2.2. Chronoamperometric tests for Cu-PANI-AC-A and Co-PANI-AC-B

To confirm the result obtained in the LSV experiments and to determine which products are actually formed in the reduction of nitrobenzene, chronoamperometric measurements in combination with GC analysis were performed for Cu-PANI-AC-A and Co-PANI-AC-B, i.e. the two electrocatalysts that gave the most promising results in terms of number of exchanged electrons and kinetic current density (Table 4). A potential of -0.75 V vs. Fc^+/Fc was chosen based on the following two criteria: (1) the current in the LSV is high enough to achieve a significant conversion in 52 h and (2) no competing reactions (e.g. H_2

Table 5

Results of GC analysis after chronoamperometry performed at -0.75 V vs. Fc/Fc^+ in a 0.3 M HClO_4 ethanolic solution (170 mL) containing 15 mM nitrobenzene for 52 h.

	Cu-PANI-AC-A	Co-PANI-AC-B
Conversion	54%	22%
Selectivity		
Aniline	82%	40%
Cyclohexylamine	0%	32%
Nitrosobenzene	3%	8%
Para-ethoxyaniline	11%	12%
Azobenzene	1%	3%
Azoxybenzene	3%	5%

evolution) are taking place at this potential. The results of these tests are summarised in Table 5. The rate of the reduction of nitrobenzene was significantly higher over Cu-PANI-AC-A, reaching 54% conversion, compared to Co-PANI-AC-B, with which 22% conversion was achieved (and accordingly higher currents were generated over Cu-PANI-AC-A during the chronoamperometric tests). At first sight, this might seem to contradict the results obtained for the kinetic current density in the LSV tests, but it can be rationalised considering that the chronoamperometric tests were carried out at higher nitrobenzene concentration (15 mM). The effect of the nitrobenzene concentration on the electrocatalysts performance was investigated by carrying out additional LSV measurements at higher concentration of nitrobenzene (15 and 30 mM, Fig. S30). The way in which the current density varies as a function of nitrobenzene concentration differs significantly between Cu-PANI-AC-A and Co-PANI-AC-B. This could be explained assuming a difference in adsorption strength and conversion rate of each of the compounds involved in the multi-step mechanism (Scheme 1) as a function of the type of electrocatalyst. This would imply that the various steps of the reduction of nitrobenzene occur at different rate on each of the two electrocatalysts, which in turn would mean that the rate law and thus the effect of nitrobenzene concentration could differ between Cu-PANI-AC-A and Co-PANI-AC-B. This hypothesis is supported by the marked difference between the physicochemical features of the two materials (*vide supra*).

Faraday's law was used to confirm the obtained values for nitrobenzene conversion by using the numbers of exchanged electrons (n) determined by the K-L equations and the total charge that passed through the cell. This gave a conversion of 55 and 21% over Cu-PANI-AC-A and Co-PANI-AC-B, respectively. The good agreement with the conversion values measured by GC (Table 5) proves that the average number of exchanged electrons determined by means of the K-L was a correct estimate. This was further evidenced by the values for the

product selectivity determined by analysing the reaction mixture after the chronoamperometric test by GC (Table 5). In the case of Cu-PANI-AC-A, a selectivity of 82% towards aniline was obtained, which is in good agreement with the value of $n = 5.8$ found using the K-L plots (Table 4). For Co-PANI-AC-B, a lower selectivity towards aniline (40%) was obtained and this is mainly due to the further reduction to cyclohexylamine (selectivity of 32%). These results again agree well with the number of exchanged electrons ($n = 9.2$) that was obtained for this system. The other major product, para-ethoxyaniline (selectivity around 10% in both cases) can be obtained through a non-electrochemical conversion of the unstable phenylhydroxylamine. This compound could not be detected by means of GC as a consequence of its oxidation to nitrosobenzene, followed by reaction with another phenylhydroxylamine to form azoxybenzene (Scheme 1) under the analysis conditions. The small amounts of azoxybenzene and nitrosobenzene that were measured (Table 5) most likely originated during the GC analysis process [7–9,18–20].

3.2.3. Stability of Cu-PANI-AC-A and Co-PANI-AC-B

Finally, the stability of Cu-PANI-AC-A and Co-PANI-AC-B was evaluated by means of cyclic voltammetry (Fig. 7). The lack of a major difference in the voltammogram between the second curve (after an initial stabilisation of the system) and the last cycle (no. 1000), indicates a high stability of the electrocatalysts under study in the acidic environment (0.3 M HClO_4), which is a promising feature for their prospective application in a fuel cell for the cogeneration of electricity and aniline.

4. Conclusions

A set of composite materials prepared from activated carbon and polyaniline and containing non-noble metals (Cu, Co or Fe) were synthesised, thoroughly characterised and evaluated as electrocatalysts for the reduction of nitrobenzene to aniline in a half-cell setup. The activity of the synthesised electrocatalysts was ranked on the basis of their onset potential and kinetic current densities, whereas the selectivity was estimated by means of the Koutecky-Levich plots and confirmed by chronoamperometry. The order of activity between the Fe-, Co- and Cu-based electrocatalysts was remarkably influenced by the synthesis parameters, with the best results among the materials prepared with low metal loading being obtained with Cu-PANI-AC-A and the best performance among the materials prepared with higher metal loading being achieved with Co-PANI-AC-B. The highest selectivity towards the desired aniline product was obtained over Cu-PANI-AC-A. The thorough physicochemical characterisation of the materials allowed determining that well-dispersed, accessible metal oxide domains (preferably in a

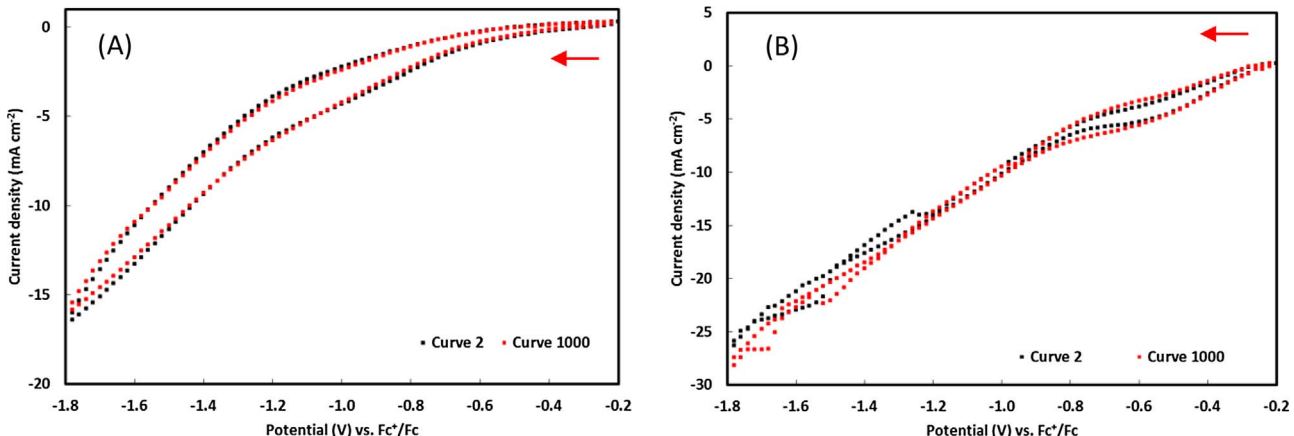


Fig. 7. Stability test of (A) CuPANI-AC-A and (B) Co-PANI-AC-B by means of cyclic voltammetry. The potential was cycled between -0.2 and -1.8 V vs. Fc/Fc^+ at a scan rate of 100 mV s $^{-1}$. Only the second curve (after initial stabilisation of the system) and the last curve are shown. Prior to the last cycle, the measurement was paused and the solution was stirred to ensure a homogeneous distribution of nitrobenzene throughout the medium.

lower oxidation state) are the main species contributing to the electrocatalytic activity in the reduction of nitrobenzene. On the other hand, larger oxides, sulphides and MeN_x species did not seem to contribute significantly to the activity. The fact that MeN_x were not identified as catalytic species in this reaction represents a notable difference with previous applications of Fe-PANI-AC electrocatalysts in the oxygen reduction reaction and in the reduction of nitric oxide to hydroxylamine [10]. The most promising electrocatalyst identified in this work, Cu-PANI-AC-A, was employed in a chronoamperometric test in which 54% conversion of nitrobenzene with a selectivity of 82% towards aniline were achieved after 52 h of reaction at $-0.75 \text{ V vs. } \text{Fc}^+/\text{Fc}$ in 0.3 M HClO_4 at room temperature. The high selectivity towards aniline represents a major improvement compared to the previous state-of-the-art electrocatalysts for this reaction (Cu/ Cu_xO supported on MWCNTs or on activated carbon), with which azoxybenzene was the major product [7,8]. The selectivity towards aniline reached with Cu-PANI-AC-A is also similar to that of the current (non-electrochemical) industrial process for the production of aniline. Importantly, cyclic voltammetry showed that the Cu-PANI-AC-A electrocatalyst also displays high stability under operating conditions. For all these reasons, the novel Cu-PANI-AC-A electrocatalyst is a promising candidate for the successful development of a fuel cell that would allow the cogeneration of electricity and aniline, as a valuable commodity product, from the reduction of nitrobenzene.

Acknowledgements

The authors acknowledge sponsoring from Flemish agency for Innovation by Science and Technology (IWT) in the frame of a Ph.D. grant (ND). We thank Gina Vanbutsele (KU Leuven) and Zhenchen Tang (University of Groningen) for helping with the N_2 physisorption measurements, Prof. Jin Won Seo for her support in the TEM analyses and the Flemish Hercules Stichting for its support in AKUL/13/19, and Dr. Benny Wouters for useful discussion.

Appendix A. Supplementary data

Supplementary data associated with this article can be found, in the online version, at <https://doi.org/10.1016/j.apcatb.2017.12.079>.

References

- [1] J. Wang, Z. Yuan, R. Nie, Z. Hou, X. Zheng, Hydrogenation of nitrobenzene to aniline over silica gel supported nickel catalysts, *Ind. Eng. Chem. Res.* 49 (2010) 4664–4669, <http://dx.doi.org/10.1021/ie1002069>.
- [2] X. Meng, H. Cheng, Y. Akiyama, Y. Hao, W. Qiao, Y. Yu, F. Zhao, S. ichiro Fujita, M. Arai, Selective hydrogenation of nitrobenzene to aniline in dense phase carbon dioxide over $\text{Ni}/\gamma\text{-Al}_2\text{O}_3$: significance of molecular interactions, *J. Catal.* 264 (2009) 1–10, <http://dx.doi.org/10.1016/j.jcat.2009.03.008>.
- [3] T. Kahl, K.-W. Schröder, F.R. Lawrence, W.J. Marshall, H. Höke, R. Jäckh, *Aniline use.pdf*, Kirk-Othmer Encycl. Chem. Technol., 5th ed., Wiley Interscience, 2011.
- [4] H. Li, Q. Zhao, Y. Wan, W. Dai, M. Qiao, Self-assembly of mesoporous Ni-B amorphous alloy catalysts, *J. Catal.* 244 (2006) 251–254, <http://dx.doi.org/10.1016/j.jcat.2006.08.025>.
- [5] S. Lee, Y. Chen, Nitrobenzene hydrogenation on Ni – P, Ni – B and Ni – P – B ultrafine materials, *J. Mol. Catal. A Chem.* 152 (2000) 213–223.
- [6] T. Niknam, M. Bornapour, A. Gheisari, B. Bahmani-Firooz, Impact of heat, power and hydrogen generation on optimal placement and operation of fuel cell power plants, *Int. J. Hydrogen Energy* 38 (2013) 1111–1127, <http://dx.doi.org/10.1016/j.ijhydene.2012.10.074>.
- [7] X. Sheng, B. Wouters, T. Breugelmans, A. Hubin, I.F.J. Vankelecom, P.P. Pescarmona, Cu/ Cu_xO and Pt nanoparticles supported on multi-walled carbon nanotubes as electrocatalysts for the reduction of nitrobenzene, *Appl. Catal. B Environ.* 147 (2014) 330–339, <http://dx.doi.org/10.1016/j.apcatb.2013.09.006>.
- [8] X. Sheng, B. Wouters, T. Breugelmans, A. Hubin, I.F.J. Vankelecom, P.P. Pescarmona, Pure and alloyed copper-based nanoparticles supported on activated carbon: synthesis and electrocatalytic application in the reduction of nitrobenzene, *ChemElectroChem* 1 (2014) 1198–1210, <http://dx.doi.org/10.1002/celec.201402015>.
- [9] B. Wouters, X. Sheng, A. Boschin, T. Breugelman, E. Ahlberg, I.F.J. Vankelecom, P.P. Pescarmona, A. Hubin, The electrocatalytic behaviour of Pt and Cu nanoparticles supported on carbon nanotubes for the nitrobenzene reduction in ethanol, *Electrochim. Acta* 111 (2013) 405–410, <http://dx.doi.org/10.1016/j.electacta>.
- [10] N. Daems, X. Sheng, Y. Alvarez-Gallego, I.F.J. Vankelecom, P.P. Pescarmona, Iron-containing N-doped carbon electrocatalysts for the cogeneration of hydroxylamine and electricity in a H_2NO fuel cell, *Green Chem.* 18 (2016) 1547–1559, <http://dx.doi.org/10.1039/C5GC02197A>.
- [11] N. Kang, J. Shin, T.S. Hwang, Y.S. Lee, A facile method for the preparation of poly(vinylidene fluoride) membranes filled with cross-linked sulfonated polystyrene, *React. Funct. Polym.* 99 (2016) 42–48, <http://dx.doi.org/10.1016/j.reactfunctopolym.2015.12.006>.
- [12] N. Daems, X. Sheng, I.F.J. Vankelecom, P.P. Pescarmona, Metal-free doped carbon materials as electrocatalysts for the oxygen reduction reaction, *J. Mater. Chem. A* 2 (2014) 4085–4110 <http://xlink.rsc.org/?DOI=c3ta14043a>.
- [13] A. Furst, R.C. Berlo, S. Hooton, Early work on nitrobenzene reduction.pdf, *Chem. Rev.* 65 (1965) 51–68.
- [14] The standard reduction potential for aniline was calculated based on the Gibbs free energy of the reagents and of the products, which is considered to be more accurate than the value reported in previous work of some of us (Refs. 7–9).
- [15] Y.P. Sun, W.L. Xu, K. Scott, A study of the electrochemical reduction of nitrobenzene to p-aminophenol in a packed bed electrode reactor, *Electrochim. Acta* 38 (1993) 1753–1759, [http://dx.doi.org/10.1016/0013-4686\(93\)85073-8](http://dx.doi.org/10.1016/0013-4686(93)85073-8).
- [16] J. Jiang, R. Zhai, X. Bao, Electrocatalytic properties of Cu-Zr amorphous alloy towards the electrochemical hydrogenation of nitrobenzene, *J. Alloys Compd.* 354 (2003) 248–258, [http://dx.doi.org/10.1016/S0925-8388\(02\)01359-2](http://dx.doi.org/10.1016/S0925-8388(02)01359-2).
- [17] Y. Chen, L. Xiong, W. Wang, X. Zhang, H. Yu, Efficient and selective electro-reduction of nitrobenzene by the nano-structured Cu catalyst prepared by an electrodeposited method via tuning applied voltage, *Front. Environ. Sci. Eng.* 9 (2015) 897–904, <http://dx.doi.org/10.1007/s11783-015-0782-1>.
- [18] A.R. Becker, L.A. Sternson, Oxidation of phenylhydroxylamine in aqueous solution: a model for study of the carcinogenic effect of primary aromatic amines, *Proc. Natl. Acad. Sci. U. S. A.* 78 (1981) 2003–2007.
- [19] G. Kokkinidis, K. Jüttner, The electrocatalytic influence of underpotential lead adsorbates on the reduction of nitrobenzene and nitrosobenzene on silver single crystal surfaces in methanolic solutions, *Electrochim. Acta* 26 (1981) 971–977, [http://dx.doi.org/10.1016/0013-4686\(81\)85065-7](http://dx.doi.org/10.1016/0013-4686(81)85065-7).
- [20] D. Groskova, M. Stolcova, M. Hronec, Reaction of N-phenylhydroxylamine in the presence of clay catalysts, *Catal. Lett.* 69 (2000) 113–116, <http://dx.doi.org/10.1023/A:1019097217875>.
- [21] X.Z. Yuan, Z.F. Ma, Q.Z. Jiang, W.S. Wu, Cogeneration of cyclohexylamine and electrical power using PEM fuel cell reactor, *Electrochim. Commun.* 3 (2001) 599–602, [http://dx.doi.org/10.1016/S1388-2481\(01\)00226-0](http://dx.doi.org/10.1016/S1388-2481(01)00226-0).
- [22] S. Jayabal, R. Ramaraj, Bimetallic Au/Ag nanorods embedded in functionalized silicate sol-gel matrix as an efficient catalyst for nitrobenzene reduction, *Appl. Catal. A Gen.* 470 (2014) 369–375, <http://dx.doi.org/10.1016/j.apcata.2013.10.056>.
- [23] A. Cyr, P. Huot, J.-F. Marcoux, G. Belot, E. Lavorin, J. Lessard, The electrochemical reduction of nitrobenzene and azoxybenzene in neutral and basic aqueous methanolic solutions at polycrystalline copper and nickel electrodes, *Electrochim. Acta* 34 (1989) 439–445, [http://dx.doi.org/10.1016/0013-4686\(89\)87023-9](http://dx.doi.org/10.1016/0013-4686(89)87023-9).
- [24] Q. Zhang, Y. Liu, S. Chen, X. Quan, H. Yu, Nitrogen-doped diamond electrode shows high performance for electrochemical reduction of nitrobenzene, *J. Hazard. Mater.* 265 (2014) 185–190, <http://dx.doi.org/10.1016/j.jhazmat.2013.11.065>.
- [25] Z.Y. Sun, Y.F. Zhao, Y. Xie, R.T. Tao, H.Y. Zhang, C.L. Huang, Z.M. Liu, The solvent-free selective hydrogenation of nitrobenzene to aniline: an unexpected catalytic activity of ultrafine Pt nanoparticles deposited on carbon nanotubes, *Green Chem.* 12 (2010) 1007–1011, <http://dx.doi.org/10.1039/C002391d>.
- [26] L.Z. Huang, H.C.B. Hansen, M.J. Bjerrum, Electrochemical reduction of nitroaromatic compounds by single sheet iron oxide coated electrodes, *J. Hazard. Mater.* 306 (2016) 175–183, <http://dx.doi.org/10.1016/j.jhazmat.2015.12.009>.
- [27] Z. Chen, Z. Wang, D. Wu, L. Ma, Electrochemical study of nitrobenzene reduction on galvanically replaced nanoscale Fe/Au particles, *J. Hazard. Mater.* 197 (2011) 424–429, <http://dx.doi.org/10.1016/j.jhazmat.2011.09.054>.
- [28] L. Chen, L. Zhang, Z. Chen, H. Liu, R. Luque, Y. Li, A covalent organic framework-based route to the in situ encapsulation of metal nanoparticles in N-rich hollow carbon spheres, *Chem. Sci.* 7 (2016) 6015–6020, <http://dx.doi.org/10.1039/C6SC01659F>.
- [29] Z. Zhang, X. Wei, Y. Yao, Z. Chen, A. Zhang, W. Li, W.D. Wu, Z. Wu, X.D. Chen, D. Zhao, Conformal coating of Co/N-doped carbon layers into mesoporous silica for highly efficient catalytic dehydrogenation–hydrogenation tandem reactions, *Small* 13 (2017) 1–8, <http://dx.doi.org/10.1002/smll.201702243>.
- [30] N. Liu, L. Ding, H. Li, M. Jia, W. Zhang, N. An, X. Yuan, N-doped nanoporous carbon as efficient catalyst for nitrobenzene reduction in sulfide-containing aqueous solutions, *J. Colloid Interface Sci.* 490 (2017) 677–684, <http://dx.doi.org/10.1016/j.jcis.2016.11.099>.
- [31] G. Wu, K.L. More, C.M. Johnston, P. Zelenay, High-performance electrocatalysts for oxygen reduction derived from polyaniline, iron, and cobalt, *Science* 332 (2011) 443–447, <http://dx.doi.org/10.1126/science.1200832>.
- [32] G. Wu, C.M. Johnston, N.H. Mack, K. Artyushkova, M. Ferrandon, M. Nelson, J.S. Lezama-Pacheco, S.D. Conradson, K.L. More, D.J. Myers, P. Zelenay, Synthesis–structure–performance correlation for polyaniline–Me–C non-precious metal cathode catalysts for oxygen reduction in fuel cells, *J. Mater. Chem.* 21 (2011) 11392–11405, <http://dx.doi.org/10.1039/c0jm03613g>.
- [33] J.C. Vickr, D. Briggs, ToF-SIMS. Materials Analysis by Mass Spectrometry, 2nd ed., IM Publications LLP, 2013.
- [34] P. Vermeiren, R. Leyens, H. Beckers, J.P. Moreels, A. Claes, The influence of manufacturing parameters on the properties of macroporous Zirfon® separators, *J. Porous Mater.* 15 (2008) 259–264, <http://dx.doi.org/10.1007/s10934-006-9084-0>.

[35] I. Herrmann, U.I. Kramm, J. Radnik, S. Fiechter, P. Bogdanoff, Influence of sulfur on the pyrolysis of CoTMPP as electrocatalyst for the oxygen reduction reaction, *J. Electrochem. Soc.* 156 (2009) B1283–B1292, <http://dx.doi.org/10.1149/1.3185852>.

[36] M. Lefvre, J.P. Dodelet, P. Bertrand, C. Electrocatalysts, B.L. Boulet, Molecular oxygen reduction in PEM fuel cell conditions: ToF-SIMS analysis of Co-based electrocatalysts, *J. Phys. Chem. B* (2005) 16718–16724, <http://dx.doi.org/10.1021/jp0529265>.

[37] M. Lefvre, J.P. Dodelet, P. Bertrand, Molecular oxygen reduction in PEM fuel cells: evidence for the simultaneous presence of two active sites in Fe-based catalysts, *J. Phys. Chem. B* 106 (2002) 8705–8713, <http://dx.doi.org/10.1021/jp020267f>.

[38] Z. Lin, G. Waller, Y. Liu, M. Liu, C.P. Wong, Facile synthesis of nitrogen-doped graphene via pyrolysis of graphene oxide and urea, and its electrocatalytic activity toward the oxygen-reduction reaction, *Adv. Energy Mater.* 2 (2012) 884–888, <http://dx.doi.org/10.1002/aenm.201200038>.

[39] J. Hoekstra, A.M. Beale, F. Soulimani, M. Versluijs-Helder, J.W. Geus, L.W. Jenneskens, Base metal catalyzed graphitization of cellulose: a combined Raman spectroscopy, temperature-dependent X-ray diffraction and high-resolution transmission electron microscopy study, *J. Phys. Chem. C* 119 (2015) 10653–10661, <http://dx.doi.org/10.1021/acs.jpcc.5b00477>.

[40] F. Vallejos-Burgos, S. Utsumi, Y. Hattori, X. García, A.L. Gordon, H. Kanoh, K. Kaneko, L.R. Radovic, Pyrolyzed phthalocyanines as surrogate carbon catalysts: initial insights into oxygen-transfer mechanisms, *Fuel* 99 (2012) 106–117, <http://dx.doi.org/10.1016/j.fuel.2012.03.055>.

[41] K.T. Lee, X. Ji, M. Rault, L.F. Nazar, Simple synthesis of graphitic ordered mesoporous carbon materials by a solid-state method using metal phthalocyanines, *Angew. Chem. – Int. Ed.* 48 (2009) 5661–5665, <http://dx.doi.org/10.1002/anie.200806208>.

[42] a Moisala, a G. Nasibulin, E.I. Kauppinen, The role of metal nanoparticles in the catalytic production of single-walled carbon nanotubes—a review, *J. Phys. – Condens. Matter.* 15 (2003) S3011, <http://dx.doi.org/10.1088/0953-8984/15/42/003>.

[43] M.S. Liao, S. Scheiner, Electronic structure and bonding in metal phthalocyanines, metal = Fe, Co, Ni, Cu, Zn, Mg, *J. Chem. Phys.* 114 (2001) 9780–9791, <http://dx.doi.org/10.1063/1.1367374>.

[44] M. Mananghaya, Hydrogen adsorption of novel N-doped carbon nanotubes functionalized with Scandium, *J. Chem. Sci.* 127 (2015) 751–759, <http://dx.doi.org/10.1016/j.jhydene.2015.05.087>.

[45] M.C. Biesinger, B.P. Payne, A.P. Grosvenor, L.W.M. Lau, A.R. Gerson, R.S.C. Smart, Resolving surface chemical states in XPS analysis of first row transition metals, oxides and hydroxides: Cr, Mn, Fe, Co and Ni, *Appl. Surf. Sci.* 257 (2011) 2717–2730, <http://dx.doi.org/10.1016/j.apsusc.2010.10.051>.

[46] L. Lozzi, S. Picozzi, S. Santucci, C. Cantalini, B. Delley, Photoemission and theoretical investigations on NO₂ doping of copper phthalocyanine thin films, *J. Electron. Spectros. Relat. Phenomena* 137–140 (2004) 101–105, <http://dx.doi.org/10.1016/j.elspec.2004.02.034>.

[47] O. Akhavan, R. Azimirad, S. Safa, E. Hasani, CuO/Cu(OH)₂ hierarchical nanostructures as bactericidal photocatalysts, *J. Mater. Chem.* 21 (2011) 9634, <http://dx.doi.org/10.1039/c0jm04364h>.

[48] A.D.S. Cells, S. Chang, M. Lu, Y. Tung, H. Tuan, Gram-scale synthesis of catalytic Co₉S₈ nanocrystal ink as a cathode, *ACS Nano* (2013) 9443–9451.

[49] R.L. Arechederra, K. Artyushkova, P. Atanassov, S.D. Minteer, Growth of phthalocyanine doped and undoped nanotubes using mild synthesis conditions for development of novel oxygen reduction catalysts, *ACS Appl. Mater. Interfaces* 2 (2010) 3295–3302, <http://dx.doi.org/10.1021/am100724v>.

[50] L. Zhu, D. Susac, M. Teo, K.C. Wong, P.C. Wong, R.R. Parsons, D. Bizzotto, K.A.R. Mitchell, S.A. Campbell, Investigation of Co₂S₃ based thin films as model catalysts for the oxygen reduction reaction, *J. Catal.* 258 (2008) 235–242, <http://dx.doi.org/10.1016/j.jcat.2008.06.016>.

[51] J. Yang, G. Zhu, Y. Liu, J. Xia, Z. Ji, X. Shen, S. Wu, Fe₃O₄-decorated Co₉S₈ nanoparticles in situ grown on reduced graphene oxide: a new and efficient electrocatalyst for oxygen evolution reaction, *Adv. Funct. Mater.* 26 (2016) 4712–4721, <http://dx.doi.org/10.1002/adfm.201600674>.

[52] Y.X. Zhou, H. Bin Yao, Y. Wang, H.L. Liu, M.R. Gao, P.K. Shen, S.H. Yu, Hierarchical hollow Co₉S₈ microspheres: solvothermal synthesis, magnetic, electrochemical, and electrocatalytic properties, *Chem. – A Eur. J.* 16 (2010) 12000–12007, <http://dx.doi.org/10.1002/chem.200903263>.

[53] Z.P. Li, W.Y. Li, H.T. Xue, W.P. Kang, X. Yang, M.L. Sun, Y.B. Tang, C.S. Lee, Facile fabrication and electrochemical properties of high-quality reduced graphene oxide/ cobalt sulfide composite as anode material for lithium-ion batteries, *RSC Adv.* 4 (2014) 37180–37186, <http://dx.doi.org/10.1039/C4ra06067a>.

[54] X. Liu, H. Liu, Y. Zhao, Y. Dong, Q. Fan, Q. Kuang, Synthesis of the carbon-coated nanoparticle Co₉S₈ and its electrochemical performance as an anode material for sodium-ion batteries, *Langmuir* 32 (2016) 12593–12602, <http://dx.doi.org/10.1021/acs.langmuir.6b02870>.

[55] T.J. Chuang, C.R. Brundle, D.W. Rice, Interpretation of the x-ray photoemission spectra of cobalt oxides and cobalt oxide surfaces, *Surf. Sci.* 59 (1976) 413–429, [http://dx.doi.org/10.1016/0039-6028\(76\)90026-1](http://dx.doi.org/10.1016/0039-6028(76)90026-1).

[56] J. Yang, H. Liu, W.N. Martens, R.L. Frost, Synthesis and characterization of cobalt hydroxide, cobalt oxyhydroxide, and cobalt oxide nanodisks, *J. Phys. Chem. C* 114 (2010) 111–119, <http://dx.doi.org/10.1021/jp908548f>.

[57] P. Chen, F. Yang, A. Kostka, W. Xia, Interaction of cobalt nanoparticles with oxygen- and nitrogen- functionalized carbon nanotubes and impact on nitrobenzene hydrogenation catalysis, *ACS Catal.* 4 (2014) 1478–1486, <http://dx.doi.org/10.1021/cs500173t>.

[58] Y. Chen, S. Zhao, Z. Liu, Influence of the synergistic effect between Co–N–C and ceria on the catalytic performance for selective oxidation of ethylbenzene, *Phys. Chem. Chem. Phys.* 17 (2015) 14012–14020, <http://dx.doi.org/10.1039/C5CP01829C>.

[59] H. Peng, Z. Mo, S. Liao, H. Liang, L. Yang, F. Luo, H. Song, Y. Zhong, B. Zhang, High performance Fe- and N- doped carbon catalyst with graphene structure for oxygen reduction, *Sci. Rep.* 3 (2013) 1765, <http://dx.doi.org/10.1038/srep01765>.

[60] M. Salavati-Niasari, Synthesis, characterization of cobalt(II) complex nanoparticles encapsulated within nanoreactors of zeolite-Y and their catalytic activities, *J. Mol. Catal. A Chem.* 310 (2009) 51–58, <http://dx.doi.org/10.1016/j.molcata.2009.05.018>.

[61] X. Wang, Q. Xiang, B. Liu, L. Wang, T. Luo, D. Chen, G. Shen, TiO₂ modified FeS nanostructures with enhanced electrochemical performance for lithium-ion batteries, *Sci. Rep.* 3 (2013) 1–8, <http://dx.doi.org/10.1038/srep02007>.

[62] A.E. Bocquet, T. Mizokawa, T. Saitoh, H. Namatame, A. Fujimori, Electronic structure of 3d-transition-metal compounds by analysis of the 2p core-level photoemission spectra, *Phys. Rev. B* 46 (1992) 3771–3784, <http://dx.doi.org/10.1103/PhysRevB.46.3771>.

[63] G. Panzner, B. Egert, The bonding state of sulfur segregated to α-iron surfaces and on iron sulfide surfaces studied by XPS, AES and ELS, *Surf. Sci.* 144 (1984) 651–664, [http://dx.doi.org/10.1016/0039-6028\(84\)90125-0](http://dx.doi.org/10.1016/0039-6028(84)90125-0).

[64] T. Yamashita, P. Hayes, Analysis of XPS spectra of Fe²⁺ and Fe³⁺ ions in oxide materials, *Appl. Surf. Sci.* 254 (2008) 2441–2449, <http://dx.doi.org/10.1016/j.apsusc.2007.09.063>.

[65] K. Asami, K. Hashimoto, The X-ray photo-electron spectra of several oxides of iron and chromium, *Corros. Sci.* 17 (1977) 559–570, [http://dx.doi.org/10.1016/S0010-938X\(77\)80002-4](http://dx.doi.org/10.1016/S0010-938X(77)80002-4).

[66] M. Descotes, F. Mercier, N. Thromat, C. Beaucaire, M. Gautier-Soyer, Use of XPS in the determination of chemical environment and oxidation state of iron and sulfur samples: constitution of a data basis in binding energies for Fe and S reference compounds and applications to the evidence of surface species of an oxidized py, *Appl. Surf. Sci.* 165 (2000) 288–302, [http://dx.doi.org/10.1016/S0169-4322\(00\)00443-8](http://dx.doi.org/10.1016/S0169-4322(00)00443-8).

[67] K. Gong, F. Du, Z. Xia, M. Durstock, L. Dai, Nitrogen-doped carbon nanotube arrays with high electrocatalytic activity for oxygen reduction, *Science* 323 (2009) 760–764, <http://dx.doi.org/10.1126/science.1168049>.

[68] H.W. Liang, W. Wei, Z.S. Wu, X. Feng, K. Müllen, Mesoporous metal-nitrogen-doped carbon electrocatalysts for highly efficient oxygen reduction reaction, *J. Am. Chem. Soc.* 135 (2013) 16002–16005, <http://dx.doi.org/10.1021/ja407552k>.

[69] D. Eisenberg, W. Stroek, N.J. Geels, C.S. Sandu, A. Heller, N. Yan, G. Rothenberg, A simple synthesis of an N-doped carbon ORR catalyst: hierarchical micro/meso/macroporosity and graphitic shells, *Chem. – A Eur. J.* 22 (2016) 501–505, <http://dx.doi.org/10.1002/chem.201504568>.